The Journal of Chemical Physics ARTICLE pubs.aip.org/aip/jcp

Q-Chem/CP2K software interface for projection-based, pseudoperiodic wavefunction-in-DFT embedding

Cite as: J. Chem. Phys. 165, 164112 (2026); doi: 10.1063/5.0361468
Submitted: 20 September 2026 • Accepted: 1 October 2026 •
Published Online: 23 October 2026

View Online Export Citation CrossMark

Ar. M. Fonlon,[1] Elena Kolodzeiski,[2,3] Kay Carter-Fenk,[1,4,5] Dustin R. Broderick,[1,a)] Christopher J. Mundy,[5] Christopher J. Stein,[3,6,b)] and John M. Herbert[1,c)]

AFFILIATIONS

[1] Department of Chemistry and Biochemistry, The Ohio State University, Columbus, Ohio 43210, USA
[2] Department of Chemistry, Quantum Chemistry, Technical University of Darmstadt, Darmstadt, Germany
[3] Department of Chemistry and Catalysis Research Center, School of Natural Sciences, Technical University of Munich, Garching, Germany
[4] Department of Chemistry, University of Pittsburgh, Pittsburgh, Pennsylvania 15260, USA
[5] Pacific Northwest National Laboratory, Richland, Washington 99354, USA
[6] Atomistic Modeling Center, Munich Data Science Institute, Technical University of Munich, Garching, Germany

Note: This paper is part of the Special Topic on Electronic Structure Software 2.0.
[a)] **Present address:** Department of Chemistry, University of Chicago, Chicago, Illinois 60637, USA.
[b)] **Author to whom correspondence should be addressed:** christopher.stein@tum.de
[c)] herbert@chemistry.ohio-state.edu

ABSTRACT

We report an implementation of projection-based quantum embedding that combines periodic density functional theory in the CP2K code with correlated wavefunction calculations in the Q-Chem program. Using this interface, correlated wavefunction methods can be applied to a subset of molecular orbitals, selected in an automated manner based on a user-defined list of nuclei, with an embedding potential that provides electronic coupling to the remaining orbitals that comprise the environment. Our implementation uses exact projection, without the need for any level-shift operator, and is "pseudoperiodic" in the sense that periodic boundary effects are implicit in the orbitals used in the (non-periodic) wavefunction calculation. Convergence tests demonstrate that computed properties are faithful to the corresponding periodic quantities, provided that the high-level subsystem is spatially localized and small, relative to the periodic simulation cell. Spectroscopic examples for aqueous chromophores demonstrate converged results using a very limited subset of water molecules in the simulation cell, decoupling the choice of excited-state method and basis set from the functional that is used to propagate ground-state *ab initio* molecular dynamics. Solvatochromic shifts for aqueous uracil are converged using equation-of-motion coupled-cluster theory, without the need for solvent molecules in the wavefunction calculation, and the embedded calculation captures solvent effects that are absent in gas-phase "microhydration" studies. Additional applications include adsorption of CO on a slab model of Si(100) and bond dissociation in a one-dimensional periodic polymer. In both of the latter cases, the system/environment partition crosses a covalent bond; these applications demonstrate that pseudoperiodic embedding can be applied to realistic systems in materials science.

© 2026 Author(s). All article content, except where otherwise noted, is licensed under a Creative Commons Attribution (CC BY) license (https://creativecommons.org/licenses/by/4.0/). https://doi.org/10.1063/5.0361468

23 October 2026 11:51:08

I. INTRODUCTION

The current workhorse for condensed-phase quantum chemistry (QC) is periodic density functional theory (pDFT). Such calculations are expensive, but one may generate hybrid DFT trajectories of ~100 ps, for a unit cell containing ~100 atoms, in a few weeks of time on just a few compute nodes.[1] Periodic implementations of some correlated wavefunction methods are now available,[2–18] but applications have mostly been limited to small unit cells. Even for the least expensive correlated wavefunction methods, such as second-order Møller–Plesset perturbation theory (MP2), calculations at the scale described above remain cripplingly expensive.[19]

Nevertheless, DFT manifests an undesirable lack of systematic improvability. Delocalization error remains a problem,[20] especially for open-shell systems,[21–25] even for hybrid functionals.[25–28] Range-separated and long-range corrected (LRC) hybrid functionals[29–35] have done much to eliminate problems with spurious, low-energy charge-transfer excitations in time-dependent (TD-)DFT,[32,36–39] especially when used in conjunction with "optimal tuning."[40–45] However, progress in producing functionals with more accurate excitation energies has been slow.[46] Condensed-phase TDDFT spectra remain exquisitely sensitive to the fraction of exact exchange that is included in the functional,[26,47,48] as do the one-electron Kohn–Sham energy levels.[49–52]

Thus, alternative approaches to condensed-phase spectroscopy and reactivity remain necessary. Even with wavefunction methods replacing DFT, however, conventional quantum mechanics/molecular mechanics (QM/MM) schemes are cumbersome for simulating electronic spectra of aqueous chromophores. Exchange of solvent molecules between the QM and MM regions is a persistent problem,[53] and spurious excitations to the QM/MM interface appear when the QM region is small.[26,54] As compared to atomistic methods, continuum treatments of the solvent struggle to reproduce oscillator strengths.[55]

Projection-based embedding theory (PBET) represents an alternative atomistic approach at a "QM/QM" level.[56–58] Using a projection operator to identify a subset of molecular orbitals (MOs) that are strongly associated with particular user-defined atoms, in an automated way, a correlated wavefunction method can be employed using this subset of MOs as its active space. The remaining MOs are described using DFT. A schematic view is shown in Fig. 1, which emphasizes similarities with the multilayer "ONIOM" technique[59] that is often used for both QM/MM and QM/QM calculations.

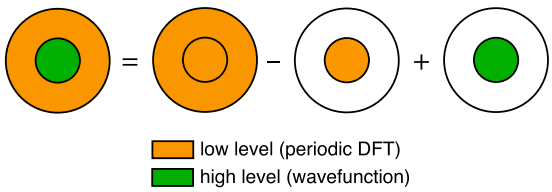


FIG. 1. Schematic view of a subtractive (ONIOM-style) partition into high- and low-level subsystems. Within PBET, the high- and low-level subsystems are subsets of the MOs for the entire supersystem, coupled by a one-electron embedding potential.

A variety of alternative quantum embedding methods have been described in the literature.[5,60–68] These include pseudoperiodic treatments ("finite cluster in periodic environment"), which are similar in spirit to the present approach,[69–81] and which have applications to solid-state materials.[82–86] In our view, the PBET formalism is particularly straightforward to implement, and it is the only embedding strategy that is pursued here. Unlike the purely subtractive ONIOM method, or embedded versions of the many-body expansion,[87,88] PBET includes electronic coupling between the wavefunction calculation and its DFT environment, by means of a one-electron embedding potential as described in Sec. II A.

In PBET, the projection operator that is used to select the wavefunction's active space also enforces orthogonality between these active MOs and the remaining (environment) MOs. This obviates the need for nonadditive kinetic energy schemes,[89] as required in subsystem DFT,[61,68] which limits the latter to weakly interacting subsystems. No such restriction exists in PBET, where even bond-breaking examples have been considered.[56,64]

However, other sources of error can affect the accuracy of PBET.[90] Functional-dependent inaccuracies in the DFT description of the environment, such as density-driven errors or self-interaction error, can lead to spurious charge-transfer.[91] The latter becomes especially pronounced for long-range polarization interactions, in ionic systems (for example), or when solute–solvent charge-transfer excitations are described.[92] Finally, PBET relies on the assumption of well-defined orbital partition, which is a severe challenge when the MOs are intrinsically delocalized, as in metallic systems.[93,94]

The present work reports an implementation of wavefunction-in-pDFT embedding based on an interface between Q-Chem[95] and CP2K.[96] The latter is selected due to its efficient (and still improving[97,98]) implementation of exact exchange under periodic boundary conditions,[99,100] making for relatively efficient calculations using hybrid density functionals. Hybrid functionals are crucial for spectroscopic applications, in order to position water's bandgap appropriately: semilocal functionals afford bandgaps of 4–5 eV,[101–104] whereas the correct position is 7–9 eV.[105–107] If the gap is underestimated, then excitations that ought to be localized on the chromophore (plus, perhaps, a few nearest-neighbor solvent molecules) can access the solvent's conduction band, leading to artificial delocalization in the excited state.[101] Along similar lines, spurious mixing of defect states can occur in solid-state pDFT applications, due to anomalously low bandgaps predicted by semilocal functionals.[108]

Although a fully periodic implementation of PBET has been reported,[64] the present version is "pseudoperiodic" in the sense that the wavefunction part of the calculation (performed using Q-Chem) does not employ periodic boundaries. Our implementation is a "cluster in periodic environment" embedding scheme, and most of our workflow uses the finite "cluster" basis for the high-level subsystem. For the periodic portion of the calculation in CP2K, only the Γ-point is computed. Nevertheless, the MOs computed using pDFT (in CP2K) for the high-level region retain an imprint of periodic boundaries, as does the embedding potential. This approach is straightforward, and convergence tests will demonstrate its potential. Proof-of-concept applications using wavefunction-in-DFT methods to model the electronic spectroscopy of condensed-phase chromophores demonstrate that converged solvatochromic shifts can be obtained in this manner, and that there are

23 October 2026 11:51:08

© Author(s) 2026

important contributions to solvent effects that are not captured by microhydration, meaning gas-phase wavefunction calculations that include a few explicit water molecules. Materials science applications suggest that the results are not overly sensitive to the size of the high-level region.

II. THEORY

Below, we describe a multilayer model and an embedding potential that together define the PBET approach (Sec. II A). Then, we discuss options for partitioning the MOs into high- and low-level subsystems (Sec. II B). Our software implementation is described in Sec. II C.

A. Projection-based embedding

PBET can be formalized in a manner that emphasizes its parallels to the subtractive ONIOM-style approach. Using "H" and "L" to indicate high- and low-level subsets of the supersystem's MOs, whose determination is discussed in Sec. II B, the model is

$$E = \underbrace{E_{\mathrm{low}}[\boldsymbol{\gamma}^{\mathrm{H}\oplus\mathrm{L}}] - E_{\mathrm{low}}[\boldsymbol{\gamma}^{\mathrm{H}}] + E_{\mathrm{high}}[\tilde{\Psi}^{\mathrm{H}}]}_{\text{ONIOM-style}} + E_{\mathrm{emb}}. \tag{1}$$

The first three terms correspond to the diagrams in Fig. 1, and the final term (E_{emb}) introduces electronic coupling between the subsystems and is explicated below. We use $\boldsymbol{\gamma}$ to indicate a one-electron density matrix; $\boldsymbol{\gamma}^{\mathrm{H}}$ (for the high-level subsystem) and $\boldsymbol{\gamma}^{\mathrm{H}\oplus\mathrm{L}}$ (for the entire system) are both computed at the low level of theory. In the present work, that means DFT although the formalism in Eq. (1) does not require this choice.

The quantity $\tilde{\Psi}^{\mathrm{H}}$ in Eq. (1) represents the wavefunction for the high-level subsystem, which collapses to the corresponding density matrix,

$$\tilde{\Psi}^{\mathrm{H}} \rightarrow \tilde{\boldsymbol{\gamma}}^{\mathrm{H}}. \tag{2}$$

In the special case of DFT-in-DFT embedding using two different exchange–correlation functionals, $\tilde{\Psi}^{\mathrm{H}}$ is simply the Kohn–Sham determinant for the high-level subsystem and could be replaced by the corresponding density matrix ($\tilde{\boldsymbol{\gamma}}^{\mathrm{H}}$) in Eq. (1).

The H/L partition is achieved by projecting the variational degrees of freedom for subsystem H out of the supersystem H ⊕ L. In the original version of PBET introduced by Manby and Miller,[56,89] this was accomplished by means of a level-shift operator with a large (but otherwise essentially arbitrary) value for the level shift itself. The version of PBET that is implemented in Q-Chem does not employ any level shift and is based on exact projection, recognizing that the one-electron density matrix is a projection operator onto the occupied space. More precisely, if $\boldsymbol{\gamma}^{\mathrm{L}}$ is expressed in the nonorthogonal atomic orbital (AO) basis, with overlap matrix $\mathbf{S}$, then $\boldsymbol{\gamma}^{\mathrm{L}}\mathbf{S}$ is the appropriate projector onto the low-level subsystem. The Fock matrix for subsystem H, embedded in bath L, is obtained by exact projection onto the high-level subsystem,[57]

$$\tilde{\mathbf{F}}^{\mathrm{H-in-L}} = (\mathbf{1} - \mathbf{S}\boldsymbol{\gamma}^{\mathrm{L}})\mathbf{F}(\mathbf{1} - \boldsymbol{\gamma}^{\mathrm{L}}\mathbf{S}). \tag{3}$$

Here, $\mathbf{F}$ is the low-level Fock matrix for the supersystem (H ⊕ L). Elsewhere,[109] this exact projection approach has been discussed in terms of solution of the Huzinaga equation.[110]

The embedding term in Eq. (1) is

$$E_{\mathrm{emb}} = \mathrm{tr}\big[(\tilde{\boldsymbol{\gamma}}^{\mathrm{H}} - \boldsymbol{\gamma}^{\mathrm{H}})\mathbf{v}_{\mathrm{emb}}\big]. \tag{4}$$

The embedding potential, $\mathbf{v}_{\mathrm{emb}}[\boldsymbol{\gamma}^{\mathrm{H}}, \boldsymbol{\gamma}^{\mathrm{L}}]$, is a functional of the density matrices for both subsystems, evaluated at the lower level of theory. Writing the Fock matrix as $\mathbf{F} = \mathbf{h} + \mathbf{G}$ in the usual way,[111] where $\mathbf{h}$ and $\mathbf{G}[\boldsymbol{\gamma}]$ are the one- and two-electron contributions, respectively, this embedding potential can be expressed as

$$\mathbf{v}_{\mathrm{emb}} = \mathbf{G}_{\mathrm{low}}[\boldsymbol{\gamma}^{\mathrm{H}\oplus\mathrm{L}}] - \mathbf{G}_{\mathrm{low}}[\boldsymbol{\gamma}^{\mathrm{H}}]. \tag{5}$$

The bottleneck step in the construction of $\mathbf{v}_{\mathrm{emb}}$ is equivalent to one Fock build on the full system (H ⊕ L) at the low level of theory, to obtain $\mathbf{G}_{\mathrm{low}}[\boldsymbol{\gamma}^{\mathrm{H}\oplus\mathrm{L}}]$ in Eq. (5).

B. Orbital partition

PBET requires a scheme to partition the MOs in an automated way. While there have been some specialized schemes developed to do this for specific applications, such as charge-transfer-to-solvent excitations,[57] the standard schemes are based on a list of user-identified nuclei to define the high-level region. This takes advantage of the atom-centered nature of the AO basis set to associate basis functions with selected atoms. In Q-Chem's implementation, this identification can use either Pipek–Mezey localization,[112,113] as in the original Manby–Miller implementation of PBET,[56,89] or else the *subsystem projected AO decomposition* (SPADE) algorithm.[58,93,114]

1. Pipek–Mezey localization

In the Pipek–Mezey approach, orbitals ϕ_i are localized by maximizing the functional

$$\mathcal{L}[\{\phi_i\}] = \sum_{A}^{\mathrm{atoms}} \sum_{i}^{\mathrm{occ}} \left|Q_i^A\right|^2, \tag{6}$$

where

$$Q_i^A = \frac{1}{2}\sum_{\mu\in A}\sum_{\nu}\left(c_{\nu i}^{*}S_{\nu\mu}c_{\mu i} + c_{\mu i}^{*}S_{\mu\nu}c_{\nu i}\right) \tag{7}$$

is the contribution from occupied orbital ϕ_i to the Mulliken population on atom A.[112] (An analogous localization procedure exists for the virtual MOs.[113]) Upon convergence of the localization procedure, the quantity

$$\sigma_i^{\mathrm{PM}} = \sum_{A\in\mathrm{H}} Q_i^A \tag{8}$$

provides a measure of the contribution that localized orbital i makes to the high-level region defined by atoms $A \in \mathrm{H}$.

2. SPADE

Problems with Pipek–Mezey localization in solids have been noted,[93,115,116] and the examples presented in Sec. III use the SPADE algorithm instead.[114] This procedure begins with Löwdin orthogonalization of the occupied MOs of the pDFT calculation on H ⊕ L. Letting $\mathbf{C}_{\mathrm{occ}}$ indicate the rectangular matrix of occupied MO coefficients $c_{\mu i}$ in the AO basis, the corresponding coefficient matrix in the orthogonalized basis is

$$\tilde{\mathbf{C}}_{\mathrm{occ}} = \mathbf{S}^{1/2}\mathbf{C}_{\mathrm{occ}}. \tag{9}$$

23 October 2026 11:51:08

© Author(s) 2026

We denote the orthogonalized AOs as $|\bar{\mu}\rangle$ and construct a projection operator

$$\hat{P} = \sum_{\bar{\mu} \in \mathrm{H}} |\bar{\mu}\rangle\langle\bar{\mu}| \tag{10}$$

onto the space spanned by AOs $\bar{\mu} \in \mathrm{H}$ that are centered on atoms that the user has identified as defining the high-level region.

The operator $\hat{P}$ in Eq. (10) is used to project the orthogonalized MOs for the entire system $(\mathrm{H} \oplus \mathrm{L})$ onto the model system,

$$\bar{\mathbf{C}}^{\mathrm{H}}_{\mathrm{occ}} = \mathbf{P}\bar{\mathbf{C}}_{\mathrm{occ}}. \tag{11}$$

We construct the singular value decomposition (SVD) of the projected MO coefficients,

$$\bar{\mathbf{C}}^{\mathrm{H}}_{\mathrm{occ}} = \mathbf{L}\boldsymbol{\Sigma}\mathbf{R}^{\dagger}, \tag{12}$$

where $\mathbf{L}$ and $\mathbf{R}$ denote the left and right singular vectors of $\bar{\mathbf{C}}^{\mathrm{H}}_{\mathrm{occ}}$, respectively. The matrix $\boldsymbol{\Sigma}$ is diagonal and contains the singular values,

$$\boldsymbol{\Sigma} = \begin{pmatrix} \sigma_1 & 0 & 0 & \cdots \\ 0 & \sigma_2 & 0 & \cdots \\ 0 & 0 & \ddots & \end{pmatrix}_{n_{\mathrm{o}} \times n_{\mathrm{o}}}, \tag{13}$$

with one σ_i for each of n_{o} occupied MOs. These singular values can be used in the same way as the quantities σ_i^{PM} defined in Eq. (8), namely, to weight the importance of each occupied MO to the description of the high-level subsystem.

The matrix $\mathbf{R}$ in Eq. (12) can be decomposed into its span and its null space,[57]

$$\mathbf{R} = \mathbf{R}_{\mathrm{span}} \oplus \mathbf{R}_{\mathrm{null}}, \tag{14}$$

with the latter defined by the zero singular values. Rather than defining $\mathbf{R}_{\mathrm{null}}$ using the strictly zero singular values, however, we can generalize this partition to use a threshold value τ_{SVD}, placing the ith column of $\mathbf{R}$ into $\mathbf{R}_{\mathrm{null}}$ if $\sigma_i < \tau_{\mathrm{SVD}}$. Doing so defines orbitals for the high- and low-level subsystems:[57]

$$\mathbf{C}^{\mathrm{H}}_{\mathrm{occ}} = \bar{\mathbf{C}}^{\mathrm{H}}_{\mathrm{occ}}\mathbf{R}_{\mathrm{span}}, \tag{15a}$$

$$\mathbf{C}^{\mathrm{L}}_{\mathrm{occ}} = \bar{\mathbf{C}}^{\mathrm{H}}_{\mathrm{occ}}\mathbf{R}_{\mathrm{null}}. \tag{15b}$$

Effectively, the SVD in Eq. (12) distills the information content of $\bar{\mathbf{C}}_{\mathrm{occ}}$ by rank-ordering the low-level MOs according to which ones are best supported by orthogonalized basis functions $\bar{\mu} \in \mathrm{H}$.

Figure 2 provides several examples of the SVD-based SPADE partition. For main-group bond breaking [Fig. 2(a)], as considered in the original design of SPADE,[114] the singular values σ_i exhibit a sudden drop in magnitude beyond an effective minimal basis. This means five MOs for the –OH moiety of ethanol and 16 MOs for the =CH–CH=CH–CH= moiety that is selected for the retinal chromophore in Fig. 2(a), corresponding to the atoms involved in *trans* → *cis* photoisomerization. In these examples, the largest sequential gap $\sigma_{i+1} - \sigma_i$ can be used to select the active space in an obvious way.[114]

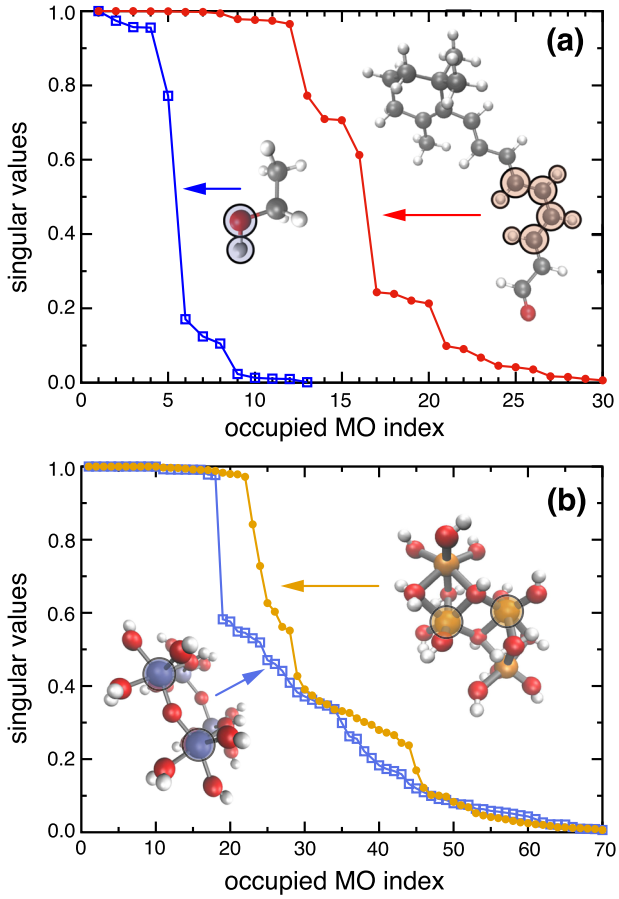


FIG. 2. Examples of singular values σ_i generated by the SPADE algorithm, ranking the importance of the occupied MOs for describing a user-defined set of atoms. (a) SPADE singular values for the indicated atoms in ethanol and retinal. (b) Singular values for $Ti_4O_{18}H_{20}$ and $Fe_4O_{16}H_{20}$, which are cluster models of anatase titania (TiO_2) and hematite (Fe_2O_3). Two of the four transition metal atoms are selected as the high-level region in the latter examples, as indicated. All calculations were performed at the PBE0/def2-TZVP level.

In contrast, when SPADE is applied to finite cluster models of titania (TiO_2) and hematite (Fe_2O_3), the singular values decay more slowly as a result of the more delocalized electronic structure in these systems [Fig. 2(b)]. Especially for hematite, it is less obvious which active orbitals should be selected. Nevertheless, the criterion $\sigma_i > \tau_{\mathrm{SVD}}$ provides a controlled approximation with a limiting behavior, where the high-level wavefunction method is applied to all the MOs as $\tau_{\mathrm{SVD}} \to 0$. In practice, it might be necessary to perform several calculations, with different values of τ_{SVD}, to assess the convergence of the property of interest with respect to the selected orbital space. If that property is insensitive to the choice of τ_{SVD}, then no further effort is required. If a systematic dependence remains, then the property of interest can be extrapolated to the $\tau_{\mathrm{SVD}} \to 0$ limit using several calculations with different values of τ_{SVD}.

Especially for systems with singular value profiles such as those in Fig. 2(b), a fixed value of τ_{SVD} may lead to a qualitative change in the orbital space along a trajectory, possibly leading to

23 October 2026 11:51:08

© Author(s) 2026

discontinuities in the potential energy surface. This is always a possibility in active-space methods,[117–125] and a variety of "even-handed" orbital selection techniques have been developed to address this issue.[93,125–127] Importantly, the orbitals have well-defined weights (σ_i) that can assist in this process. These weights should be continuous functions of the nuclear coordinates.

3. Virtual orbitals

Section II B 2 involves only the occupied MOs and leaves open the question of which virtual orbitals should be used. In previous work, we have simply used the entire virtual space for TDDFT-in-DFT embedding,[57] which is sometimes feasible because the cost of TDDFT scales only as $\mathcal{O}(n_o^2 n_v^2)$, where n_o and n_v are the number of occupied and virtual orbitals, respectively. Furthermore, a cutoff can be used to discard the high-energy virtual MOs in the canonical representation.[128]

For correlated wavefunction-in-DFT calculations, however, the scaling with respect to n_v becomes prohibitive, e.g., $\mathcal{O}(n_o^2 n_v^4)$ for coupled-cluster theory with single and double substitutions (CCSD). In such cases, truncation of the virtual space is required, and we accomplish this using the concentric localization scheme of Claudino and Mayhall.[58,129] Like SPADE, this procedure is SVD-based and provides an importance weighting for a set of non-canonical MOs.

Starting from the canonical virtual MOs for H ⊕ L, with MO coefficients $C_{\mu a}$, the first step is to project these onto the high-level subsystem. This defines virtual orbitals with coefficients

$$C_{\mu a'} = \sum_{\lambda \in \mathrm{H}} (\mathbf{S}^{-1})_{\mu\lambda} \sum_{\sigma \in \mathrm{H}\oplus\mathrm{L}} S_{\lambda\sigma} C_{\sigma a}. \tag{16}$$

The MO index on the left (a') has been given a prime to indicate the one-to-one correspondence with the canonical virtual indices a.[58] Equation (16) defines a set of transformed virtual orbitals, whose coefficients will be expressed in matrix form as $\mathbf{C}'_{\mathrm{vir}}$. The overlap between those orbitals and the canonical set is then subjected to an SVD,[58,129]

$$(\mathbf{C}'_{\mathrm{vir}})^\dagger \mathbf{S} \mathbf{C}_{\mathrm{vir}} = \mathbf{U}\boldsymbol{\Sigma}'\mathbf{V}^\dagger. \tag{17}$$

The most important virtual orbitals can be selected based on the singular values in $\boldsymbol{\Sigma}'$.

Coefficients for this minimal set of valence virtuals can be expressed as

$$\mathbf{C}_0 = \mathbf{C}_{\mathrm{vir}} \mathbf{V}_{\mathrm{span}}, \tag{18}$$

where $\mathbf{V}_{\mathrm{span}}$ represents the n_{basis} singular vectors with the largest singular values. [Here, $\mathbf{V} = \mathbf{V}_{\mathrm{span}} \oplus \mathbf{V}_{\mathrm{null}}$ in analogy with Eq. (14).] Limiting the virtual space to the n_{basis} virtual MOs in $\mathbf{C}_0$ has been called the "single-ζ" approximation.[129] To avoid confusion with basis-set terminology, however, we will refer to $\mathbf{C}_0$ as the minimal set of virtual orbitals, or one shell.

The remaining virtual orbitals (outside of the minimal set) are defined by coefficients

$$\mathbf{C}_{\mathrm{null},0} = \mathbf{C}_{\mathrm{vir}} \mathbf{V}_{\mathrm{null}}. \tag{19}$$

To extend beyond the minimal number, Claudino and Mayhall[129] suggest examining the singular values defined by

$$\mathbf{C}_0^\dagger \mathbf{F} \mathbf{C}_{\mathrm{null},0} = \mathbf{U}_0 \boldsymbol{\Sigma}_0 \mathbf{V}_0^\dagger \tag{20}$$

and taking the n_{basis} largest singular values (in $\boldsymbol{\Sigma}_0$) to define an additional set of virtual orbitals,

$$\mathbf{C}_1 = \mathbf{C}_{\mathrm{null},0} \mathbf{V}_{\mathrm{span},0}, \tag{21}$$

where $\mathbf{V}_0 = \mathbf{V}_{\mathrm{span},0} \oplus \mathbf{V}_{\mathrm{null},0}$. The set $\mathbf{C}_0 \oplus \mathbf{C}_1$ defines what Claudino and Mayhall call the "double-ζ approximation," but we will call it simply $\mathbf{C}_0 \oplus \mathbf{C}_1$ or two concentric shells. This truncation affords excellent recovery of ground-state correlation energies computed at the MP2-in-DFT level.[129] The procedure could be extended to additional concentric shells, but we will not do so.

C. Implementation

For the present work, we developed an "external embedding" interface within Q-Chem. It allows the program to read MO data from other electronic structure codes, although its present incarnation is limited to reading CP2K data. The workflow for this interface, which does not modify the CP2K code, is shown in Fig. 3. It uses Q-Chem to generate a CP2K-formatted basis function file and a snippet of a CP2K input file that can be used to ensure that all paths are correct. The latter file is printed to the Q-Chem output file and must be extracted for use as a CP2K input file. CP2K is run as a separate calculation (i.e., externally), possibly with additional hardware-specific parameters. As compared to calling CP2K as a library, this workflow requires user intervention but allows CP2K to be parallelized across nodes without being constrained by Q-Chem's single-node architecture. (Q-Chem v. 7 does include some multi-node parallelism,[130] but that functionality is not used here.)

A successful CP2K calculation generates a formatted text file containing the MO coefficients and energy levels. A PBET calculation in Q-Chem will detect this file and parse its format. Then, Q-Chem rebuilds and subsequently diagonalizes the low-level supersystem Fock matrix, in order to construct the embedding potential and to evaluate $E_{\mathrm{low}}[\boldsymbol{\gamma}^{\mathrm{H}}]$ in Eq. (1). This is followed by SPADE partition of the MOs and selection of those with the largest singular values, which are then optimized (to obtain $\tilde{\boldsymbol{\gamma}}^{\mathrm{H}}$) using a wavefunction method in Q-Chem. The latter can include TDDFT (Sec. III A 2).

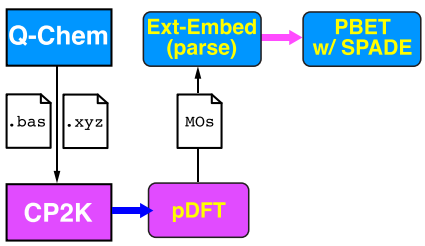


FIG. 3. Workflow associated with the Q-Chem/CP2K external embedding ("Ext-Embed") interface. Supersystem MOs are obtained from a pDFT calculation in CP2K and then passed to Q-Chem. Those MOs are parsed by the external embedding interface in Q-Chem and the SPADE partition is performed within that program, followed by a high-level (wavefunction) calculation on the active MOs.

23 October 2026 11:51:08

© Author(s) 2026

Notably, the low-level Fock matrix computed in Q-Chem does not include periodic effects from the environment. As such, the low-level effects that are subtracted out in Eq. (1), as well as the embedding potential $\mathbf{v}_{\text{emb}}$, are missing fully periodic interactions. However, the initial MOs come from the periodic calculation, and this likely prevents certain artificial polarization that we have sometimes observed in large but finite cluster calculations, starting from a gas-phase guess.[94] We consider the present approach to be "pseudoperiodic," and its utility is demonstrated with examples in Sec. III.

The pseudoperiodic nature of the embedding does mean that the user-specified subsystem atoms of interest should reside at the center of the unit cell in order to prevent edge effects. (Solvent molecules may extend beyond the unit cell in order to preserve bonds.) This is not done automatically. Some tools for manipulating the unit cell can be found elsewhere.[88]

III. APPLICATIONS

We first consider several applications involving aqueous systems (Sec. III A), as these are common targets for *ab initio* molecular dynamics (MD) using pDFT. Covalent periodic systems are considered in Sec. III B. All calculations were performed using CP2K v. 2025.1.[96] The external embedding interface is available in Q-Chem v. 7.0.[95] The absolute localization scheme that is described in Sec. III B 2 will be released with Q-Chem v. 7.0.1.

A. Aqueous systems

For a molecular liquid, the SPADE algorithm selects orbitals that localize onto individual molecules, and it suffices to specify the high-level subsystem in terms of what molecules it contains. Nevertheless, the MOs on one molecule do hybridize with its nonbonded neighbors, because the underlying MOs for H ⊕ L were computed from a full-system DFT calculation. In particular, this means that solvent–chromophore hybridization is included even if the high-level region contains only the chromophore.

In what follows, we first present convergence tests for the pseudoperiodic embedding approximation (Sec. III A 1) using neat liquid water. Following that, we examine two spectroscopic examples involving aqueous chromophores. First, TDDFT-in-pDFT embedding is applied to the aqueous hydroxyl radical (Sec. III A 2), where configurations featuring a two-center, three-electron hemibond have been implicated in the liquid structure[131–135] and in the valence spectroscopy,[26,27,136] yet the description of that hemibonded state is sensitive to delocalization error in DFT.[26,27,137–139] In a second example, equation-of-motion (EOM-)CCSD is used for the high-level subsystem (Sec. III A 3). In particular, we use EOM-CCSD-in-pDFT embedding to estimate solvatochromic shifts for the S_1 and S_2 excited states of aqueous uracil and to establish whether "microhydration" is sufficient to describe these effects.

1. Convergence tests: DFT-in-pDFT

We first describe two sets of convergence tests for neat liquid water, using the Perdew–Burke–Ernzerhof (PBE) functional for both the high- and low-level regions in an effort to evaluate the physical consistency of the pseudoperiodic embedding scheme. In these tests, the model high-level region consists of a single water molecule in periodic unit cells of increasing size, ranging from L = 6 to 20 Å [Fig. 4(a)]. These tests establish the impact of truncating the Hamiltonian for this active subsystem in a non-periodic Q-Chem calculation. Convergence is quantified using the gradient with respect to orbital rotations,[111] which is reported as the error from the direct inversion in the iterative subspace (DIIS) procedure.[140] The DIIS error measures stationarity of the pDFT MOs (or lack thereof) when they are used as guess orbitals for a non-periodic DFT calculation using the same functional.

Results in Fig. 4(b) demonstrate that the initial DIIS error (for the single H_2O molecule that defines the subsystem) decreases monotonically as the environment region increases in size. As more water molecules are included in the environment, corresponding to larger simulation cell sizes L, the model region becomes further

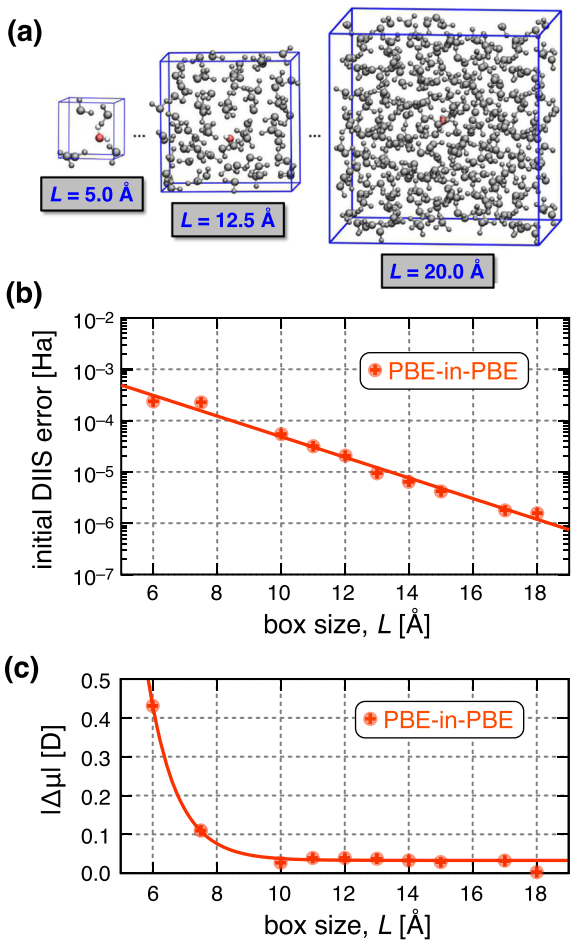


FIG. 4. Validation and convergence tests at the PBE/def2-SVP level. (a) Water boxes of increasing size, with a single H_2O molecule selected as the high-level subsystem. (b) Initial SCF convergence error for MO optimization of the high-level subsystem, serving as an indicator of the accuracy of the periodic CP2K MOs within the non-periodic Q-Chem embedding framework. (c) Absolute deviation of the subsystem (H_2O) dipole moment ($|\Delta\mu|$), relative to a reference computed from the corresponding supersystem pDFT calculation. The value of μ is computed for the H_2O molecule in question using CM5 atomic charges obtained from optimized MOs. The line in (b) and the curve in (c) are guides for the eye.

23 October 2026 11:51:08

© Author(s) 2026

polarized by the periodic MOs, and a better description of periodicity is obtained. Correspondingly, the quality of the MOs used as an initial guess for the non-periodic embedding calculations improves.

The same convergence can be illustrated by considering the dipole moment (μ) for the single-H_2O subsystem. We estimate μ using CM5 atomic point charges,[141] computed using subsystem-optimized (PBE-in-PBE) MOs. Results in Fig. 4(c) demonstrate that this dipole moment converges to the bulk pDFT value (for the central H_2O molecule) as L increases.

Together, these tests suggest that a box with $L \approx 13$ Å is sufficient to recover the essential periodic influences on the active subsystem and to minimize finite-size artifacts. At that point, the error in the H_2O dipole moment is $|\Delta\mu| \approx 0.04$ D, and the DIIS error in the energy is $\approx 10^{-5}$ Ha. The latter value is comparable to the convergence threshold for single-point self-consistent field (SCF) energy calculations in Q-Chem.

Building on this, we performed a secondary stress test to evaluate sensitivity with respect to the size of the subsystem. Considering a cubic box with $L = 15.2$ Å that contains 128 water molecules, we systematically increased the number of water molecules in the high-level region, up to a radius of $r = 7.5$ Å [Fig. 5(a)]. Results in Fig. 5(b) demonstrate that the initial DIIS error increases monotonically with the radius of the high-level region. As the subsystem size increases, the active sphere (of radius r) approaches the boundaries of the simulation cell ($r \approx L/2$), where the CP2K orbitals were initially influenced by MOs of the periodic image cell. Those images are absent in the non-periodic Q-Chem calculation, and the embedding potential cannot fully compensate, so the transferred orbitals become a progressively poorer initial guess, as quantified by the rising DIIS error as a function of r.

Ultimately, however, the quality of the initial guess is of secondary importance. The relevant question is whether the converged electronic structure of the active system correctly reproduces the properties of the chemically relevant site. This question is addressed by considering the dipole moment of the central water molecule and its deviation from a bulk CP2K reference value [Fig. 5(c)], computed using CM5 charges as indicated above. Here, PBE-in-PBE embedding serves as a particularly stringent test case, since it should precisely reproduce the supersystem result in the limit of an exact embedding potential. In fact, $|\Delta\mu|$ remains essentially constant ($|\Delta\mu| \approx 0.03$ D) across the entire range of subsystem radii. This confirms that the local electronic structure of the central molecule is consistently reproduced, independent of the active system size.

Figure 5(d) extends this test by treating the active region and the environment at different levels of theory and examining convergence of the O(1s) orbital eigenvalue for the central water molecule. The active region is described using the range-separated SRC1-R1 functional,[47] which is parameterized for K-edge spectroscopy and can be used to obtain accurate core-orbital energy levels.[142] The environment is described using PBE. The value of $\varepsilon_{O(1s)}$ converges already at the smallest active system size to a value distinctly different from the reference PBE-in-PBE value. This indicates that the improved description of core orbital energies by the SRC1-R1 functional is effectively captured. Moreover, the value of $\varepsilon_{O(1s)}$ remains stable across all tested radii, demonstrating robustness for DFT′-in-DFT embedding.

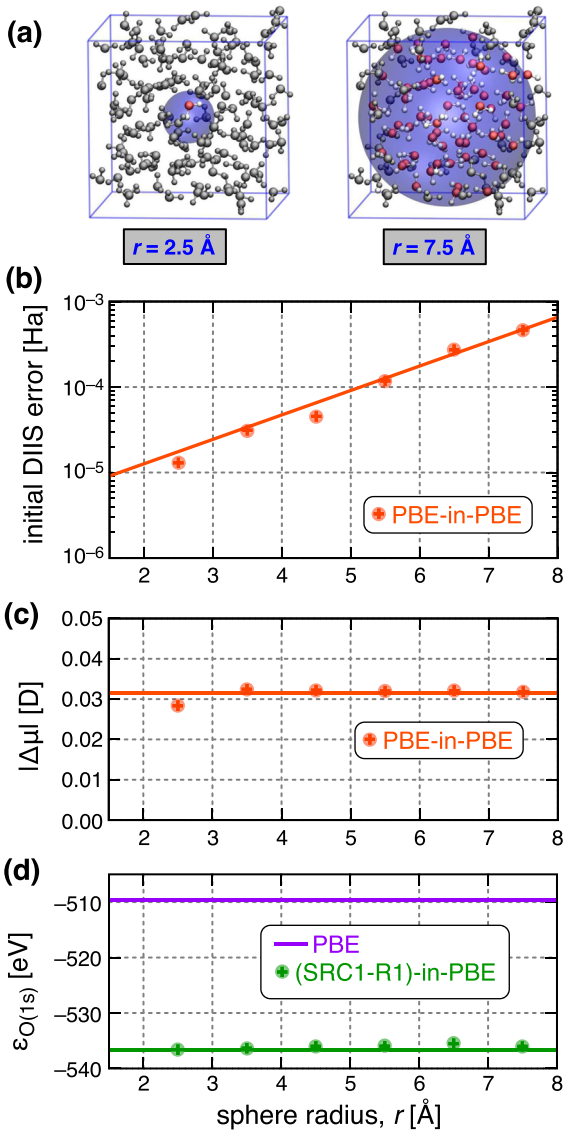


FIG. 5. Convergence tests with respect to active system size, for a water box with cell parameter $L = 15.2$ Å. (a) Illustration of the active region defined by a radius r. (b) Initial SCF error following MO read-in, as a function of r, reflecting the self-consistency demands of the embedding as the active system grows. (c) Deviation $|\Delta\mu|$ in the dipole moment of the central water molecule (estimated using CM5 point charges) relative to the pDFT reference value computed in the same way. (d) O(1s) orbital energy for the central H_2O molecule, computed using DFT′-in-PBE embedding, where DFT′ = PBE or SRC1-R1. The PBE-in-PBE value, $\varepsilon_{O(1s)} \approx -510$ eV, is simply the reference CP2K bulk PBE value. All calculations use the def2-SVP basis set.

These convergence tests confirm that the local properties of the central molecule are robust with respect to the size of the active region, irrespective of the level of theory applied within the embedding, provided that the overall simulation box is sufficiently large.

23 October 2026 11:51:08

© Author(s) 2026

This demonstrates the efficacy of the pseudoperiodic approach to PBET and also informs the user regarding how to select a reasonable subsystem size within the framework of wavefunction-in-pDFT embedding. One must ensure that the periodic simulation cell is sufficiently large with respect to the size of the model region.

2. Spectroscopy of OH(aq): TDDFT-in-pDFT

As a first spectroscopic application, we select the aqueous hydroxyl radical, OH(aq), whose electronic absorption spectrum exhibits a band maximum that is blueshifted by 1.4 eV relative to the $\tilde{A}\ ^2\Sigma^+ \leftarrow \tilde{X}\ ^2\Pi$ transition of the gas-phase radical.[143] It has been suggested that the latter transition is not actually responsible for the solution-phase absorption maximum,[136] which may arise instead from an intense $1b_2(H_2O) \rightarrow 2p(^\bullet OH)$ charge-transfer transition that is unique to the aqueous phase and is assigned to hemibonded configurations of the radical that are characterized by a short oxygen–oxygen distance in the $H_2O\cdots{}^\bullet OH$ contact pair.[26,27,136] These hemibonded configurations in OH(aq) have long been regarded as artifacts of self-interaction or delocalization error in DFT,[131,137] although more recent simulations suggest that early *ab initio* MD simulations of OH(aq) may have suffered from artifacts arising from too-small simulation cells.[133] Recent simulations with hybrid functionals suggest that hemibonded configurations may persist as a minority population, albeit one that plays an outsize role in the spectroscopy.[27]

For these tests, we use TDDFT-in-pDFT embedding. This fits seamlessly within the same wavefunction-in-DFT formalism insofar as linear-response TDDFT has the structure of a configuration interaction wavefunction with single substitutions only,[46,144] and we have previously considered a finite (cluster) version of this approach.[57] Here, we generalize this approach to include a pseudoperiodic treatment of the environment. Although it is possible to run TDDFT under periodic boundaries in CP2K,[145–147] an embedding approach may still be advantageous as it allows a different functional to be used for computing excitation energies, as compared to that used to propagate the ground-state *ab initio* MD using pDFT. For example, a hybrid or LRC functional might be used in TDDFT to avoid charge-transfer contamination and to position water's bandgap appropriately, with a semilocal functional used for efficient ground-state dynamics. In such a scenario, periodic exact exchange is needed only for those snapshots that are used to obtain an absorption spectrum, not at every time step.

An *ab initio* MD trajectory for $(OH)(H_2O)_{63}$ at the PBE/def2-TZVP level, in a unit cell with $L = 12.42$ Å, was taken from previous work,[27] where it was run at $T = 370$ K. Here, we computed an absorption spectrum from 600 snapshots sampled every 25 fs, applying TDDFT with the LRC-ωPBE functional to a high-level subsystem defined by a radius of 4.5 Å around the radical. (This amounts to 18.8 ± 1.9 water molecules in the TDDFT subsystem.) The range separation parameter in LRC-ωPBE is set to $\omega = 0.38$ bohr^{-1} using the optimal tuning procedure based on the ionization energy theorem of DFT.[41] As in previous work,[45] we refer to this functional as LRC-ω_{IE}PBE to denote the system-specific, tuned value of ω.

In previous work,[57] we demonstrated that embedding affords stable excitation spectra from snapshot to snapshot, despite fluctuations in the number of solvent molecules that are included in the TDDFT region, with embedding errors that are much smaller than step-to-step fluctuations in the excitation energy itself. In Fig. 6, we decompose the absorption spectra of $OH(H_2O)_{63}$ into different contributions based on the number of water molecules that are in the TDDFT subsystem in a given snapshot. These spectra are not normalized, i.e., what is plotted is the absolute oscillator strength from the TDDFT calculations, and the apparently low intensity for the $(OH)(H_2O)_{24}$ contribution is a result of there being only one snapshot (out of 600) having that many water molecules in the TDDFT subsystem. The absorption maxima are reasonably consistent across subsystem sizes.

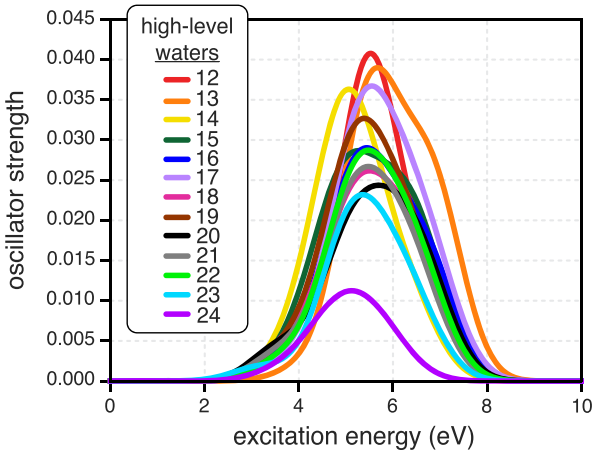


FIG. 6. Absorption spectra for OH(aq) computed using TD-LRC-ω_{IE}PBE-in-PBE embedding, decomposed into various contributions based on the number of water molecules included in the TDDFT calculation. The average number of water molecules in the TDDFT calculation is 18.8 ± 1.9. Absorption spectra were computed using 15 excited states per snapshot, weighting the transition energies by oscillator strength and broadening using a 0.6 eV Gaussian. All calculations use the def2-TZVP basis set.

The absorption spectrum for the total ensemble is plotted in Fig. 7 alongside experimental absorption intensities at selected wavelengths.[148] This comparison demonstrates the excellent consistency of the TDDFT-in-pDFT spectrum despite fluctuations in the size of the TDDFT region. Furthermore, the embedded spectrum is a good match to a spectrum computed by applying TDDFT to the full $(OH)(H_2O)_{63}$ unit cell, treated as a finite cluster. The latter spectrum, which is taken from Ref. 27, used a smaller basis set (6-31++G*) due to the large size required, whereas embedding enables a high-quality spectrum to be obtained using a much smaller number of the surrounding water molecules.

Previous theoretical studies of the OH(aq) absorption spectrum demonstrate that instantaneous configurations exhibiting a small transfer of ground-state spin density from $^\bullet OH$ to H_2O play an outsize role.[26,27] This spin-density transfer also provides an electronic (as opposed to geometrical) definition of the hemibonded configurations that support a $1b_2(H_2O) \rightarrow 2p(^\bullet OH)$ charge-transfer transition.

Following previous work,[26,27] we apply Mulliken analysis to the spin density $\rho_{\mathrm{spin}} = \rho_\alpha - \rho_\beta$, in order to quantify the spin charge $s(OH)$ on the radical. We then partition the ensemble, using a numerical cutoff for $s(OH)$ that was determined to be a proxy for hemibonded geometries.[26,27] The hemibonded subset, defined by the

23 October 2026 11:51:08

© Author(s) 2026

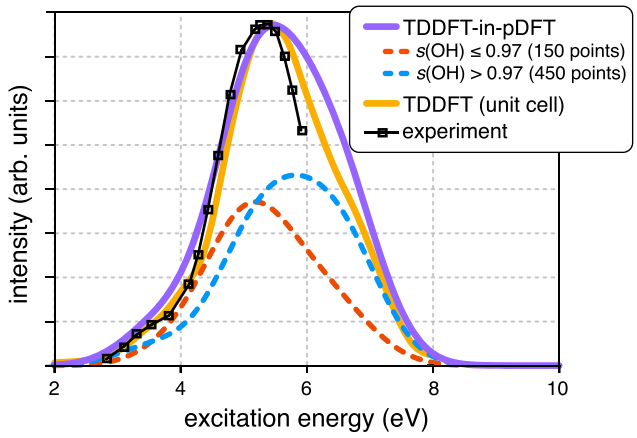


FIG. 7. Absorption spectra for OH(aq) computed using TD-LRC-ω_{IE}PBE and juxtaposed with experimental data from Ref. 148. The TDDFT-in-pDFT spectrum uses def2-TZVP for both levels of theory and applies TDDFT to a subsystem defined by a 4.5 Å radius around the radical, using 15 excited states per snapshot and 0.6 eV Gaussian broadening. Also shown are a spectrum obtained from applying TD-LRC-ω_{IE}PBE/6-31++G* to the entire unit cell and a decomposition of the TDDFT-in-pDFT spectrum into sub-ensembles based upon the radical's spin charge. That decomposition employs a cutoff value for $s(\mathrm{OH})$ that is indicative of hemibonded configurations. Note the 1:3 population ratio of the two sub-ensembles.

criterion $s(\mathrm{OH}) \leq 0.97$, is just 25% of the total population of the ensemble yet supports a roughly equal integrated oscillator strength as compared to the 75% of the ensemble with $s(\mathrm{OH}) > 0.97$, for which the spin density is almost completely localized on the $^{\bullet}$OH moiety; see Fig. 7.

This application demonstrates how a variety of wavefunction-like tools (including TDDFT) can be brought to bear on a hard-won *ab initio* MD trajectory as a post-processing step. The subsequent spectral analysis can employ alternative functionals (different from the one used for ground-state dynamics) and higher-quality basis sets, because it only requires a high-level calculation on a limited subset of solvent molecules. In Sec. III A 3, we explore a similar application using a correlated many-body wavefunction for the high-level subsystem.

3. Spectroscopy of uracil(aq): EOM-CCSD-in-pDFT

As a second spectroscopic application, we consider EOM-CCSD-in-pDFT embedding for the S_1 and S_2 states of aqueous uracil, Ura(aq). EOM-CCSD-in-DFT embedding has previously been considered for EOM-CCSD excitation energies in finite aqueous clusters,[149] and the present approach provides an alternative that can be made consistent with ground-state *ab initio* MD simulations.

Geometries for these calculations were sampled from a classical MD simulation using the AMBER99 force field.[150] Snapshots for EOM-CCSD-in-pDFT calculations were extracted at regular intervals, and the embedding calculations were performed using the PBEh(40) functional (with 40% exact exchange), which sets the water bandgap appropriately.[1,151] We will compare these results to gas-phase EOM-CCSD calculations on microhydrated clusters, $(\mathrm{Ura})(\mathrm{H_2O})_n$, with $n = 5$ and $n = 10$ water molecules. Geometries for the cluster calculations were taken from the same trajectory by selecting the n water molecules closest to uracil and deleting the rest, but otherwise keeping the same geometry. Thus, the geometry of the cybotactic region is the same in both the finite cluster calculations and the EOM-CCSD-in-pDFT embedding calculations, so that results of both can reasonably be juxtaposed along the entire trajectory.

Vertical excitation energies computed at regular intervals along the MD trajectory, for the $S_1(n\pi^*)$ and $S_2(\pi\pi^*)$ states of the chromophore, are shown in Fig. 8. These results use the def2-SVP basis set, but results using 6-311G* are almost identical, as demonstrated

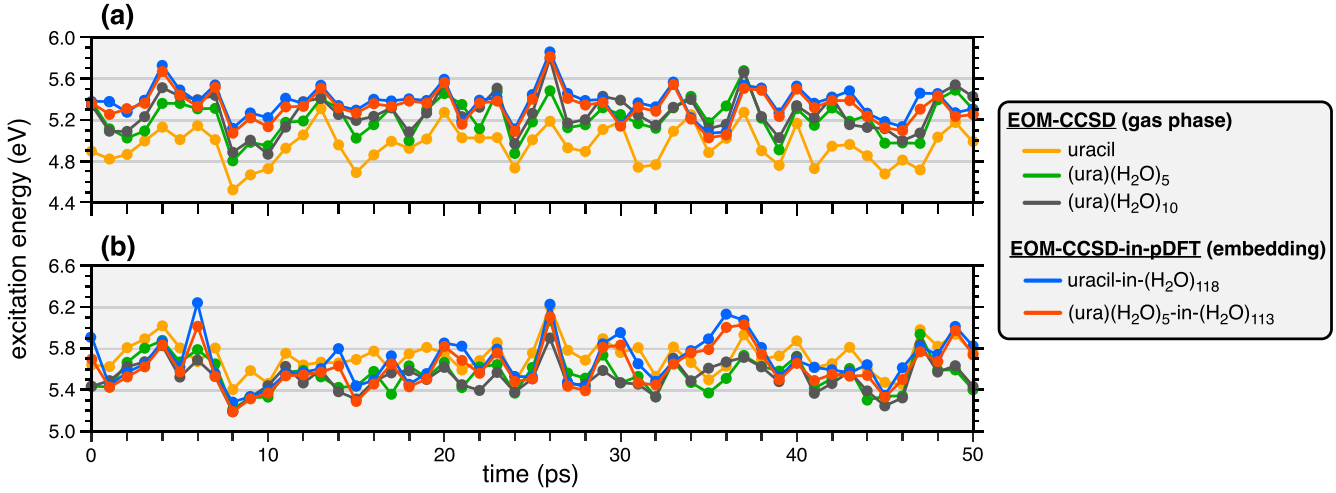


FIG. 8. Vertical excitation energies for the (a) $S_1(n\pi^*)$ and (b) $S_2(\pi\pi^*)$ states of aqueous uracil, evaluated along a classical MD trajectory. The legend explains the methods used: either gas-phase EOM-CCSD applied to microhydrated $(\mathrm{Ura})(\mathrm{H_2O})_n$ clusters ($n = 0, 5, 10$), or EOM-CCSD-in-pPBEh(40) embedding, with two different high-level regions. All calculations use the def2-SVP basis set. For the embedding calculations, two concentric shells of virtual orbitals were used ($\mathbf{C}_0 \oplus \mathbf{C}_1$).

23 October 2026 11:51:08

© Author(s) 2026

TABLE I. EOM-CCSD excitation energies for hydrated uracil.[a]

		Excitation energy (eV)				
		$Ura(H_2O)_n$ (microhydrated)			$Ura(H_2O)_n$-in-$(H_2O)_{118-n}$ (embedded)[b]	
State	Basis set	$n = 0$	$n = 5$	$n = 10$	$n = 0$	$n = 5$
S_1	def2-SVP[c]	4.95	5.21	5.27	5.37	5.33
S_2	def2-SVP[c]	5.72	5.54	5.52	5.68	5.62
S_1	6-311G*	4.98	5.23	5.27	5.32[c]	5.30[d]
S_2	6-311G*	5.64	5.49	5.49	5.70[c]	5.64[d]

[a] Averaged across 50 ps of simulation data, as in Fig. 8.
[b] PBEh(40) functional.
[c] $\mathbf{C}_0 \oplus \mathbf{C}_1$ truncation of the virtual space, meaning two concentric shells or $2n_{basis}$ virtual MOs.
[d] Minimal set ($\mathbf{C}_0$) of n_{basis} virtual orbitals.

in the statistical summary that appears in Table I. As expected,[152,153] solvent effects on the $^1\pi\pi^*$ excitation energy are modest, but they are more substantial for the $^1n\pi^*$ state, where there is a significant blueshift upon microhydration that increases in the embedded calculations. (The EOM-CCSD result for isolated uracil is also shown in Fig. 8, in order to establish the magnitude of the solvatochromic shift.) EOM-CCSD-in-pDFT results are presented using a high-level region that consists of either the chromophore only, or else $(Ura)(H_2O)_5$, keeping the five closest water molecules in the high-level region. Those two calculations are in excellent agreement across the MD trajectory, to within an average of ≤0.06 eV (Table I) using either of two basis sets and two different virtual orbital truncation schemes, either $\mathbf{C}_0$ (only) or $\mathbf{C}_0 \oplus \mathbf{C}_1$, as described in Sec. II B 3. This outstanding agreement indicates that convergence has been achieved without the need for any water molecules in the high-level region.

Let us comment briefly on the cost of these calculations. For the $(Ura)(H_2O)_5$-in-$(H_2O)_{113}$ embedding, we had to constrain the virtual MOs to the single shell defined by $\mathbf{C}_0$ in Eq. (18). A scheme with two concentric shells of virtual orbitals ($\mathbf{C}_0 \oplus \mathbf{C}_1$) has been recommended in order to converge ground-state correlation energies,[129] and Fig. 9 shows results for the same Ura(aq) systems using the def2-SVP basis set and the $\mathbf{C}_0 \oplus \mathbf{C}_1$ truncation scheme. These results are extremely similar to the 6-311G* results with the minimal set (Fig. 8), suggesting that demands on the virtual space are reduced for excitation energies, at least for localized valence excited states.

Timing data for the EOM-CCSD portion of the calculation are shown in Fig. 10. When two concentric shells of virtual orbitals are used, the $Ura(H_2O)_5$-in-$(H_2O)_{113}$ calculation is considerably more expensive than the corresponding gas-phase $Ura(H_2O)_5$ calculation although the embedding calculation also captures solvation effects that are missing in the gas-phase calculation. While the timing result might seem puzzling at first, it can be understood based on the number of virtual MOs, which is $n_v^H = n_{basis}^H - n_o^H$ for a gas-phase calculation on the high-level subsystem. For an embedding calculation using the same subsystem, the number of virtual MOs is n_{basis} if one shell is used ($\mathbf{C}_0$) or $2n_{basis}$ for two shells ($\mathbf{C}_0 \oplus \mathbf{C}_1$). For

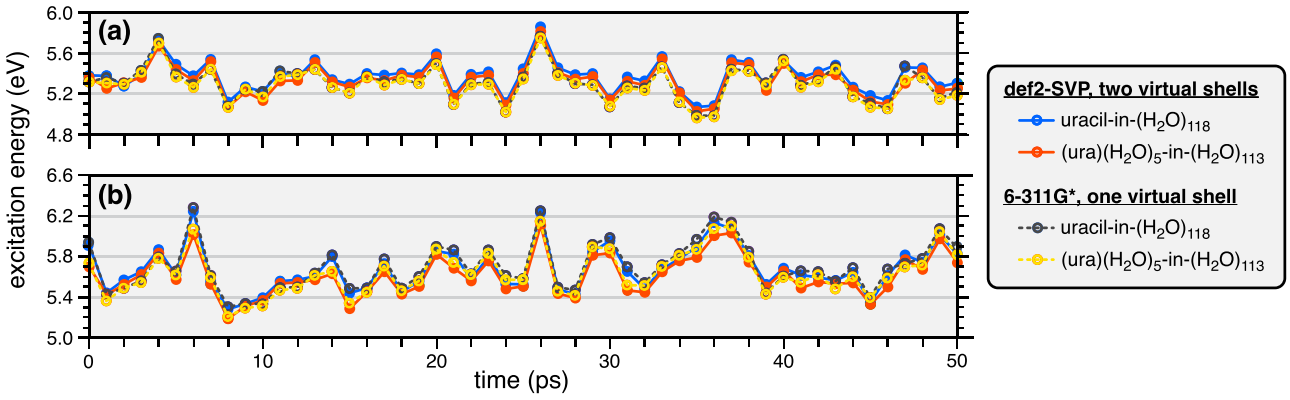


FIG. 9. Vertical excitation energies for the (a) $S_1(n\pi^*)$ and (b) $S_2(\pi\pi^*)$ states of aqueous uracil, computed using EOM-CCSD-in-PBE(40) embedding with two different basis sets. The def2-SVP data are the same as those of Fig. 8 and use $\mathbf{C}_0 \oplus \mathbf{C}_1$ for the virtual orbitals. The 6-311G* results use $\mathbf{C}_0 \oplus \mathbf{C}_1$ for uracil-in-$(H_2O)_{118}$ but use one shell of virtual orbitals ($\mathbf{C}_0$ only) for $Ura(H_2O)_5$-in-$(H_2O)_{113}$.

23 October 2026 11:51:08

© Author(s) 2026

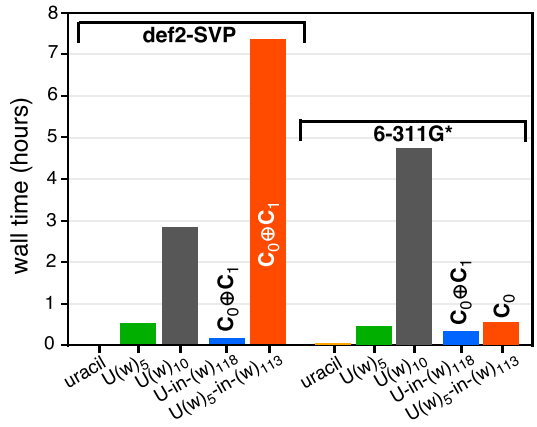


FIG. 10. Wall-time cost for the EOM-CCSD portion of the gas-phase and the embedded calculations on hydrated uracil. Data were obtained on 48 threads of a dedicated node (Dell Intel CPU Max 9470) with 128 GB of available memory. These data represent the most expensive single snapshot for gas-phase $Ura(H_2O)_{10}$. All of the embedding calculations employ two concentric shells of virtual orbitals ($\mathbf{C}_0 \oplus \mathbf{C}_1$ truncation) except for $Ura(H_2O)_5$-in-$(H_2O)_{113}$, which uses only one shell ($\mathbf{C}_0$).

$Ura(H_2O)_5$-in-$(H_2O)_{113}$ in the 6-311G* basis set, where only $\mathbf{C}_0$ is used, the timings are similar to the gas-phase $Ura(H_2O)_5$ calculation because the number of virtual MOs is more comparable.

Our results indicate that neither the second shell of virtual MOs nor the explicit water molecules in the high-level region are necessary. This reduces the cost of the embedding calculation to something comparable to gas-phase $Ura(H_2O)_5$.

B. Extended systems

So far, we have only considered systems and properties that are predominantly governed by noncovalent interactions. A major strength of PBET, however, is its ability to partition systems across covalent bonds. It does so by partition of the MOs, which are hybridized according to the chemical bonding of the whole system, rather than using link atoms (as in most QM/MM calculations) or relying on frozen orbitals at the high-level/low-level boundary. For extended materials, including polymers, a description of the periodic environment is often crucial, as it may substantially influence the electronic structure even for local properties. For systems with delocalized electronic structure, such as semiconductor materials, PBET avoids the need for pseudopotential "caps" around a finite cluster model. Although there are successful reports of such approaches in the literature,[154–157] our experience suggests that this approach requires considerable care and cannot be regarded as "black-box."

Chulhai and Goodpaster previously reported a "cluster-in-periodic environment" approach to PBET,[64] in which the environment is described using pDFT with a **k**-point-dependent embedding potential. An important prerequisite of this formulation is that the active subsystem should not interact significantly with its own periodic images, which requires a sufficiently large unit cell. This additional cost, relative to a simple pDFT calculation in a smaller unit cell, is justified by the ability to treat the active cluster with high-level methods.

Our implementation adopts and simplifies the cluster-in-periodic environment approach in order to make it more straightforward and to reduce the cost. The low-level pDFT calculation is performed using CP2K, and the resulting periodic MOs are subsequently used in Q-Chem to construct the embedding potential for the active subsystem. In contrast to the formulation of Chulhai and Goodpaster,[64] which employs a freeze-and-thaw procedure in the periodic basis to pre-optimize subsystem densities in an absolutely localized monomer basis, our implementation uses the supersystem density obtained from CP2K, avoiding this additional optimization step. As such, the embedding potential is constructed and applied without periodic boundary conditions. The impact of the periodic environment is inherently encoded in the environment's MOs, however. Phenomenologically, this does not introduce any additional approximation because negligible interaction between the active subsystem and its periodic images is already a prerequisite of the cluster-in-pDFT approach. Our implementation is restricted to the Γ-point in the pDFT calculation and is, therefore, primarily suited to localized active regions with molecular-like electronic structure, embedded in a periodic material.

Below, we test our pseudoperiodic PBET approach using two test systems that were also considered by Chulhai and Goodpaster.[64] In Sec. III B 1, we consider bond-stretching in a one-dimensional polymer, using a sequence of high-level regions of different sizes and describing the remaining polymer as a one-dimensional periodic environment. In Sec. III B 2, we consider adsorption of CO to a periodic slab model of the Si(100) surface.

1. One-dimensional polymer

We first consider the neoprene polymer using a unit cell that contains two C–Cl bonds. We call this system "neoprene-2," following the notation in Ref. 64. (A neoprene-4 system, with four C–Cl moieties in the unit cell, will be considered below.) We calculate the potential energy curve for the dissociation of one C–Cl bond, using high-level regions of varying size as depicted in Fig. 11(a) and labeled (II)–(V), again following Chulhai and Goodpaster.[64]

PBE-in-LDA embedding results, where LDA denotes the local density approximation, are presented in Fig. 11(b) and are compared to reference pDFT calculations using either functional. Taking periodic PBE as the reference, we see that periodic LDA overestimates the C–Cl bond energy by 10.7 kcal/mol. For PBE-in-LDA embedding, even the smallest choice for the high-level region reduces this error to 1.9 kcal/mol. For the larger regions (III)–(V), this error is reduced below 1 kcal/mol.

B3LYP-in-LDA embedding is considered in Fig. 11(c). As above, we observe significant improvement compared to the periodic LDA calculation and convergence toward the fully periodic B3LYP result with increasing size of the active region. For the smallest subsystems, (II) and (III), the embedding results differ by 1.6 and 2.9 kcal/mol in the C–Cl bond energy, respectively, as compared to the periodic B3LYP reference. Subsystems (IV) and (V) afford results within 1 kcal/mol of the reference value. This is comparable to the 1.2 kcal/mol error that was reported in Ref. 64 using B3LYP-in-LDA embedding with subsystem (III). We consider this to be excellent agreement, given that the implementation in Ref. 64 used a fully periodic embedding potential and the freeze-and-thaw approach that was mentioned above.

23 October 2026 11:51:08

© Author(s) 2026

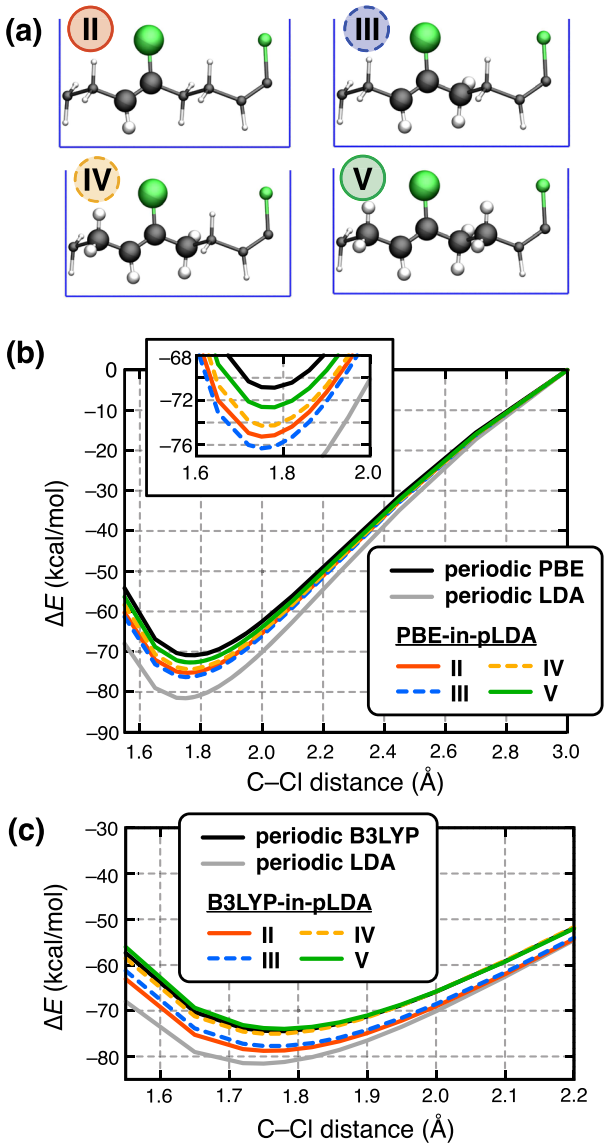


FIG. 11. PBET results for neoprene-2, a neoprene unit cell containing two C–Cl moieties. (a) Illustration of high-level regions II–V, with the high-level atoms indicated by the larger ball-and-stick models. (b) Dissociation potentials along one of the C–Cl bonds, illustrating how PBET interpolates between PBE and LDA using DFT-in-pDFT embedding. (c) Convergence behavior of B3LYP-in-LDA embedding. All calculations use the def2-SVP basis set.

At the level of DFT-in-pDFT embedding, the present approach comes with substantial computational benefit for hybrid functionals because only the high-level MOs need to be described with hybrid DFT. For model (II) of neoprene, this means 15 of the 46 occupied MOs in the unit cell are described using the hybrid functional (for spin-restricted MOs), or 20 out of 46 for model (III). This highlights the potential of DFT-in-pDFT embedding, since hybrid pDFT calculations are typically one or two orders of magnitude more expensive than semilocal pDFT, depending on the size of the unit cell. For hybrid DFT embedded in semilocal pDFT, increasing the unit-cell size to mitigate finite-size effects adds a cost that scales like the low-cost, semilocal pDFT calculation.

This advantage is even more pronounced for wavefunction-in-DFT embedding, due to the more severe computational scaling of correlated wavefunction methods with system size, but also because

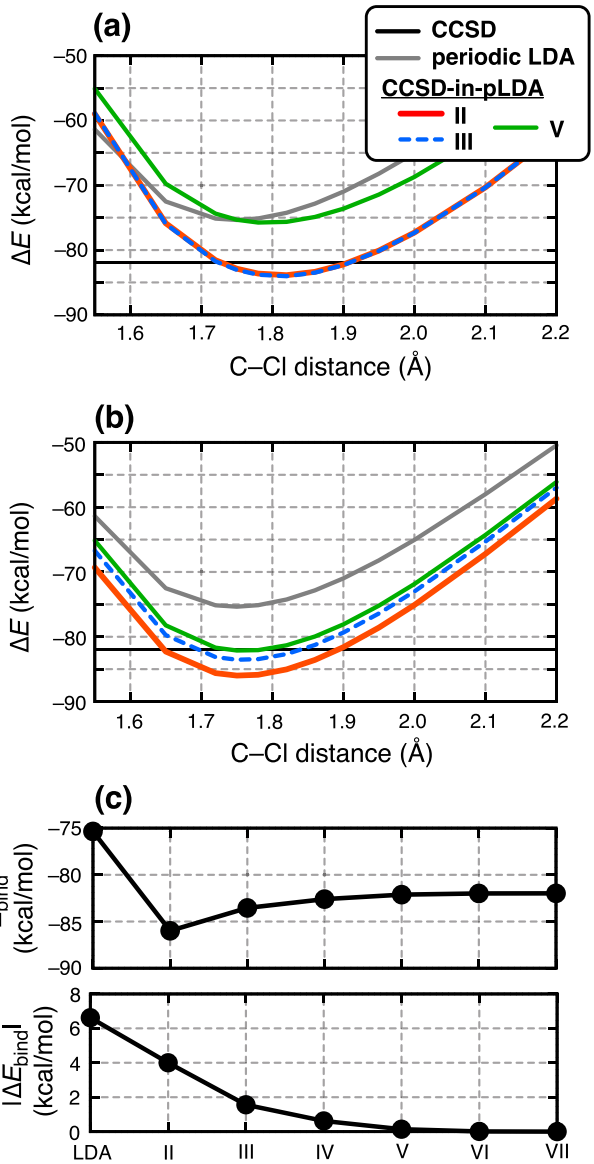


FIG. 12. CCSD-in-pDFT embedding results for C–Cl bond stretching in neoprene, using two concentric shells of virtual MOs. These results include dissociation curves for CCSD-in-pLDA embedding in (a) neoprene-2 and (b) neoprene-4, containing either two or four C–Cl moieties in the unit cell. Subsystems (II)–(V) are illustrated in Fig. 11(a) and color-coded in the same way here. (c) Convergence of the C–Cl bond energy for neoprene-4 as a function of the high-level region size (top), and difference with respect to the converged result (bottom). That converged CCSD result from (c) is indicated by the horizontal black line in (a) and (b). Calculations were performed using the 6-311G* basis set.

23 October 2026 11:51:08

© Author(s) 2026

those methods exhibit slow convergence with respect to the size of the unit cell or **k**-point sampling,[158–164] even as compared to pDFT. The problem is illustrated by the CCSD-in-LDA calculations on neoprene-2 that are shown in Fig. 12(a), which exhibit finite-size effects that do not systematically diminish with increasing size of the high-level region. The smallest subsystems, (II) and (III), deviate from a converged CCSD reference by only 2.0 and 2.1 kcal/mol, respectively, but calculations using subsystem (IV) fail to converge and those using (V) deviate by 6.2 kcal/mol from the reference value. Moreover, the dissociation minimum is also shifted relative to the periodic LDA curve. These artifacts disappear for calculations on a neoprene-4 model that has four C–Cl moieties in the unit cell. This confirms that the poor behavior in neoprene-2 is an artifact of the unit cell size.

The CCSD-in-pDFT calculations in Fig. 12 use two concentric shells of virtual orbitals ($\mathbf{C}_0 \oplus \mathbf{C}_1$ truncation). For these test cases, however, it is possible to run the calculation without any truncation of the virtual space, and doing so confirms that the two-shell result is converged to within ~0.01 kcal/mol. This is quantitatively consistent with the convergence behavior reported by Claudino and Mayhall for ground-state energies computed at the MP2-in-DFT level.[129]

Together, these results demonstrate that our pseudoperiodic implementation of PBET reliably describes both DFT-in-pDFT and correlated wavefunction-in-pDFT interactions, in systems where the high-level/pDFT partition occurs across covalent bonds. Favorable results are predicated on an adequately large unit cell, as was also the case for the solvated subsystems considered in Sec. III A. This requirement does not compromise the overall computational efficiency, however, due to favorable scaling of the low-level pDFT treatment.

2. Surface adsorption

For surface models, finite-size effects can become even more severe and we consider CO@Si(100) as a test case [Fig. 13(a)]. Using the pseudoperiodic setup described above, we were unable to obtain a smooth dissociation curve for the surface-adsorbed CO molecule due to severe convergence issues. This poor behavior arises because the MOs of the adsorbate are expressed in the basis of the supersystem and contain contributions from basis functions centered on environment atoms. When those orbitals are used in the (finite) Q-Chem SCF calculation, the absence of the corresponding periodic environment can cause the density to relax artificially into basis functions centered on the environment, which now lack adequate Pauli repulsion from periodic-image functions. This introduces spurious "dangling-bond" character into the high-level subsystem. In principle, this effect is present in the one-dimensional polymer calculations considered in Sec. III B 1 but is considerably more severe for the periodic Si(100) slab.

To address this problem, we consider an "absolutely localized" monomer basis,[64,165] in which the high-level subsystem MOs are constrained to use only those AO basis functions that are centered on the subsystem atoms. This partition begins with a SPADE decomposition of the occupied orbital space, which affords a nearly block-diagonal separation between active and environment orbitals. That is,

$$\bar{\mathbf{C}}_{\mathrm{occ}} \approx \begin{pmatrix} \bar{\mathbf{C}}^{\mathrm{H}}_{\mathrm{occ}} & \mathbf{0} \\ \mathbf{0} & \bar{\mathbf{C}}^{\mathrm{L}}_{\mathrm{occ}} \end{pmatrix}, \tag{22}$$

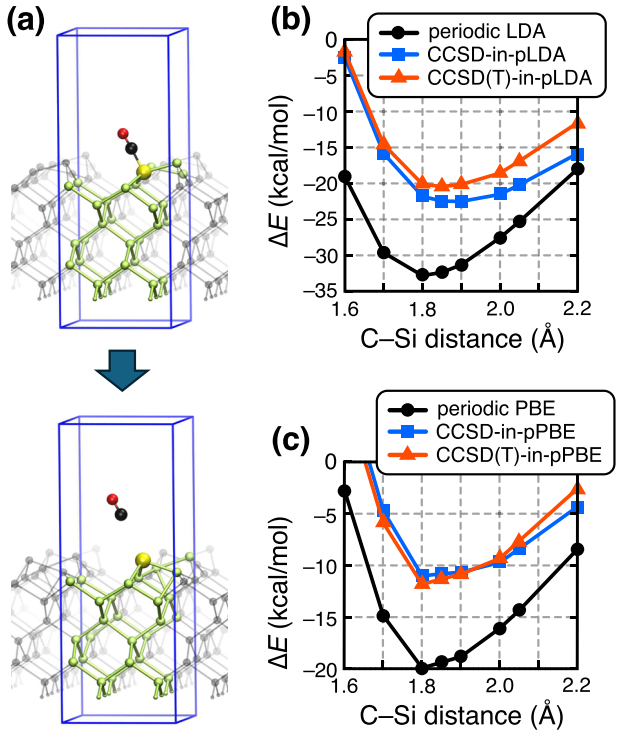


FIG. 13. CO dissociation from a Si(100) surface. (a) Illustration of the slab model that is used, with the active system (OC· · ·Si) indicated by large spheres, the periodic unit cell indicated by smaller green spheres, and periodic images in gray. (b) Dissociation curves for the OC· · ·Si bond computed using CCSD-in-pLDA and CCSD(T)-in-pLDA embedding with absolute localization. (c) Dissociation curves computed using CCSD-in-pPBE and CCSD(T)-in-pPBE embedding based on the same setup. In all of these dissociation curves, the Si(100) lattice was held rigid at the relaxed geometry obtained in the presence of the adsorbate, but binding energies are referenced to the fully relaxed, dissociated surface structure. The def2-TZVP basis set is used for Si and cc-pVTZ is used for {H, C, O}. No truncation of the virtual space is applied.

although the indicated off-diagonal blocks are not exactly zero. Absolute localization is achieved by setting them to zero. The resulting orbitals are no longer strictly orthonormal, and the Löwdin transformation is applied to $\bar{\mathbf{C}}^{\mathrm{L}}_{\mathrm{occ}}$ to restore orthogonality. To optimize the active subsystem self-consistently using only its own monomer basis, the Fock matrix $\tilde{\mathbf{F}}^{\mathrm{H-in-L}}$ must be restricted to the subsystem block and orthogonality enforced at every SCF iteration. Following the formalism of absolutely localized cluster-in-periodic embedding,[64,165] this is achieved by adding a Fermi-shifted Huzinaga-type projector to the active-fragment block of the Fock matrix. This approach prevents density leakage into the environment and ensures that the finite-cluster calculation contains only the degrees of freedom associated with the high-level subsystem. The reduced basis also provides a substantial computational advantage, particularly for correlated wavefunction-in-DFT calculations, because the expensive MO transformations are restricted to the active-region basis. For this reason, it was not necessary to truncate the virtual space for these wavefunction-in-pDFT calculations.

23 October 2026 11:51:08

© Author(s) 2026

Results using absolute localization are shown in Fig. 13(b). We obtain CO binding energies of 22.5 kcal/mol for CCSD-in-pLDA and 20.5 kcal/mol for CCSD(T)-in-pLDA. These are much larger than the experimental value of 11.6 kcal/mol,[166] and also larger than a fully periodic CCSD(T)-in-pLDA value of 13.0 kcal/mol obtained using the freeze-and-thaw method of Chulhai and Goodpaster.[64] However, our results are in much better agreement with experiment when PBE is used for the environment [Fig. 13(c)]: 11.0 kcal/mol at the CCSD-in-pPBE level and 11.8 kcal/mol at the CCSD(T)-in-pPBE level, as compared to a fully periodic CCSD(T)-in-pPBE value of 10.3 kcal/mol.[64]

Although the wavefunction-in-LDA results improve markedly on the well-known over-binding of pure periodic LDA, as documented in Fig. 13(b), the wavefunction-in-pLDA results are still significantly overbound with respect to experiment. The present calculations also exhibit greater sensitivity to the choice of low-level environment method than is observed in the fully periodic approach.[64] This difference is attributable to the simplified description of the environment density in the present calculations, which is not pre-optimized in the monomer basis. Nevertheless, good agreement with experiment can be obtained using the PBE functional for the environment, which is a reasonable choice that is widely used in applications. (LDA calculations are reported here only to make contact with analogous calculations in Ref. 64, not because LDA is a reasonable functional for practical applications.) Our approach reliably reproduces both the cluster-in-periodic environment reference and the experimental binding energy for CO@Si(100), at greatly reduced computational cost as compared to a fully periodic wavefunction treatment, and using a simplified version of PBET as compared to the use of a **k**-dependent embedding potential.

IV. CONCLUSIONS

A pseudoperiodic version of wavefunction-in-pDFT embedding, based on exact projection, has been implemented and tested using low-level calculations performed with pDFT in the CP2K code and wavefunction embedding as implemented in Q-Chem. Although the latter calculations are non-periodic, test calculations demonstrate that this introduces errors in the SCF convergence criterion that are $\sim 10^{-5}$ Ha, on par with a typical stopping criterion for SCF convergence. Thus, periodic effects remain in the low-level MOs that are used in the subsequent non-periodic wavefunction calculations, provided that the periodic simulation cell is large compared to the high-level wavefunction region.

Spectroscopic applications using EOM-CCSD-in-pDFT embedding for aqueous chromophores suggest that converged results can be obtained even when the wavefunction calculation is limited to the chromophore only, with all water molecules described using DFT. The solvatochromic shift converges only when water molecules beyond the chromophore's immediate solvation shell are included. That result is easy to reach with embedding but challenging to obtain with microhydrated EOM-CCSD alone, where the requisite explicit water molecules are cost-prohibitive.

An important caveat is that some wavefunction-in-pDFT embedding calculations reported here have been performed using basis sets such as def2-SVP and 6-311G*. In augmented double-ζ basis sets such as aug-cc-pVDZ, EOM-CCSD excitation energies sometimes exhibit convergence errors of 0.1–0.2 eV for small molecules,[167] although convergence errors are typically smaller for larger organic chromophores.[168] For the Ura(aq) calculations reported here, there is virtually no difference between def2-SVP and 6-311G* results, even with aggressive truncation of the *in situ*-optimized virtual orbitals that are used in the embedding calculation.

Our attempts to substitute def2-SVPD, def2-TZVP, cc-pVDZ, and cc-pVTZ for the EOM-CCSD-in-pDFT embedding calculations led to intractable convergence problems in CP2K. Indeed, such problems are the reason that "MOLOPT" basis sets were developed for condensed-phase DFT,[169] and versions designed for excitation energy calculations (containing additional augmentation) have been introduced recently.[170] DFT-based schemes to accelerate the basis-set convergence of wavefunction methods have also been explored.[167,171,172] These afford converged results for EOM-CCSD excitation energies in double-ζ basis sets.[167] Such methods are a natural choice for an embedding scheme that already incorporates DFT as part of its workflow, and these alternatives should be explored for spectroscopic applications of wavefunction-in-DFT going forward.

We have also considered several materials science examples where the wavefunction subsystem is covalently bonded or strongly adsorbed to its environment. Examples include C–Cl bond stretching in a one-dimensional periodic neoprene polymer and CO adsorption to a slab model of Si(100). These applications demonstrate that strongly interacting environments can yet be described by pseudoperiodic embedding. This may require an absolutely localized subsystem basis,[165] but that basis also serves to reduce the computational cost of wavefunction-in-pDFT embedding. This method is a promising way to move beyond DFT accuracy in many materials science applications, without incurring the high cost and adverse convergence behavior of fully periodic wavefunction approaches.

SUPPLEMENTARY MATERIAL

See the supplementary material for the raw data used to make the figures and for Cartesian coordinates for the systems studied.

ACKNOWLEDGMENTS

Work by A.M.F. and J.M.H. was supported by the U.S. National Science Foundation, Grant Nos. CHE-1955282 and CHE-2402361, and A.M.F. also acknowledges funding from the Ohio State Chemistry Bridge Program. E.K. was supported through the German Research Foundation (DFG) Collaborative Research Center (CRC) 1497: "Iron, upgraded!", Project No. 443703006. K.C.-F. acknowledges a Presidential Fellowship from The Ohio State University as well as additional support from the U.S. Department of Energy (DOE), Office of Workforce Development for Teachers and Scientists, and the Office of Science Graduate Student Research (SCGSR) program. The SCGSR program is administered by the Oak Ridge Institute for Science and Education (ORISE) for the DOE. ORISE is managed by ORAU under Contract No. DE-SC0014664. Work by C.J.M. was supported by the DOE, Office of Science, Basic Energy Sciences, Chemical Sciences, Geosciences, and Biosciences Division, Chemical Physics and Interfacial Sciences Program, Grant No. FWP 16249. E.K. and C.J.S. received financial support from the DFG under Germany's Excellence Strategy, Grant No. EXC

23 October 2026 11:51:08

© Author(s) 2026

2089/1-390776260, and BaCaTec Project No. 7 [2024-2]. Calculations were performed at the Ohio Supercomputer Center.[173] All opinions expressed in this paper are the authors' and may not reflect the policies and views of DOE, ORAU, or ORISE.

AUTHOR DECLARATIONS

Conflict of Interest

J.M.H. is part owner of Q-Chem Inc. and serves on its board of directors.

Author Contributions

A.M.F. and E.K. contributed equally to this work.

Ar. M. Fonlon: Data curation (equal); Formal analysis (equal); Investigation (equal); Software (supporting); Validation (equal); Writing – original draft (supporting); Writing – review & editing (supporting). **Elena Kolodzeiski**: Data curation (equal); Formal analysis (equal); Investigation (equal); Methodology (supporting); Software (supporting); Validation (equal); Writing – original draft (supporting); Writing – review & editing (equal). **Kay Carter-Fenk**: Methodology (supporting); Software (lead). **Dustin R. Broderick**: Software (supporting). **Christopher J. Mundy**: Resources (supporting); Supervision (supporting). **Christopher J. Stein**: Resources (equal); Supervision (equal); Writing – review & editing (equal). **John M. Herbert**: Conceptualization (equal); Formal analysis (equal); Funding acquisition (equal); Methodology (equal); Project administration (equal); Resources (equal); Supervision (equal); Visualization (equal); Writing – original draft (equal); Writing – review & editing (equal).

DATA AVAILABILITY

The data that support the findings of this study are available within the article and its supplementary material.

REFERENCES

[1] A. M. Fonlon, C. J. Mundy, and J. M. Herbert, "Temperature dependence of the hydrated electron's *g*-factor and persistence of a cavity-localized electron at elevated temperature," J. Am. Chem. Soc. **148**, 36675–36686 (2026).
[2] M. Del Ben, J. Hutter, and J. VandeVondele, "Second-order Møller–Plesset perturbation theory in the condensed phase: An efficient and massively parallel Gaussian and plane waves approach," J. Chem. Theory Comput. **8**, 4177–4188 (2012).
[3] M. Del Ben, J. Hutter, and J. VandeVondele, "Electron correlation in the condensed phase from a resolution of identity approach based on the Gaussian and plane waves scheme," J. Chem. Theory Comput. **9**, 2654–2671 (2013).
[4] M. Del Ben, J. Hutter, and J. VandeVondele, "Forces and stress in second order Møller-Plesset perturbation theory for condensed phase systems within the resolution-of-identity Gaussian and plane waves approach," J. Chem. Phys. **143**, 102803 (2015).
[5] D. Usvyat, L. Maschio, and M. Schütz, "Periodic and fragment models based on the local correlation approach," Wiley Interdiscip. Rev.: Comput. Mol. Sci. **8**, e1357 (2018).
[6] A. Grüneis, G. H. Booth, M. Marsman, J. Spencer, A. Alavi, and G. Kresse, "Natural orbitals for wave function based correlated calculations using a plane wave basis set," J. Chem. Theory Comput. **7**, 2780–2785 (2011).
[7] I. Y. Zhang and A. Grüneis, "Coupled cluster theory in materials science," Front. Mater. **6**, 123 (2019).
[8] A. Grüneis, "Coupled cluster and quantum chemistry schemes for solids," in *Handbook of Materials Modeling*, edited by W. Andreoni and S. Yip (Springer Nature, Switzerland, 2020), Chap. 21, pp. 453–468.
[9] A. Gallo, F. Hummel, A. Irmler, and A. Grüneis, "A periodic equation-of-motion coupled-cluster implementation applied to *F*-centers in alkaline earth oxides," J. Chem. Phys. **154**, 064106 (2021).
[10] J. McClain, Q. Sun, G. K.-L. Chan, and T. C. Berkelbach, "Gaussian-based coupled-cluster theory for the ground-state band structure of solids," J. Chem. Theory Comput. **13**, 1209–1218 (2017).
[11] A. Pulkin and G. K.-L. Chan, "First-principles coupled cluster theory of the electronic spectrum of transition metal dichalcogenides," Phys. Rev. B **101**, 241113(R) (2020).
[12] Y. Gao, Q. Sun, J. M. Yu, M. Motta, J. McClain, A. F. White, A. J. Minnich, and G. K.-L. Chan, "Electronic structure of bulk manganese oxide and nickel oxide from coupled cluster theory," Phys. Rev. B **101**, 165138 (2020).
[13] X. Wang and T. C. Berkelbach, "Absorption spectra of solids from periodic equation-of-motion coupled-cluster theory," J. Chem. Theory Comput. **17**, 6387–6394 (2021).
[14] V. A. Neufeld, H.-Z. Ye, and T. C. Berkelbach, "Ground-state properties of metallic solids from ab initio coupled-cluster theory," J. Phys. Chem. Lett. **13**, 7497–7503 (2022).
[15] T. Goldzak, X. Wang, H.-Z. Ye, and T. C. Berkelbach, "Accurate thermochemistry of covalent and ionic solids from spin-component-scaled MP2," J. Chem. Phys. **157**, 174112 (2022).
[16] A. Z. Ni, A. Rettig, and J. Lee, "Gaussian-based periodic grand canonical density functional theory with implicit solvation for computational electrochemistry," J. Chem. Theory Comput. **21**, 10961–10970 (2025).
[17] M.-F. Chen, J. Zhang, H. Q. Dinh, A. Rettig, and J. Lee, "Regularized perturbation theory for *ab initio* solids," J. Phys. Chem. Lett. **16**, 11373–11381 (2025).
[18] A. Nejad, A. Zhu, K. Sorathia, and D. P. Tew, "DLPNO-MP2 for periodic systems. I. Periodic boundary conditions," J. Chem. Phys. **163**, 214107 (2025).
[19] V. V. Rybkin, "Sampling potential energy surfaces in the condensed phase with many-body electronic structure methods," Chem. Eur. J. **26**, 362–368 (2020).
[20] K. R. Bryenton, A. A. Adeleke, S. G. Dale, and E. R. Johnson, "Delocalization error: The greatest outstanding challenge in density-functional theory," Wiley Interdiscip. Rev.: Comput. Mol. Sci. **13**, e1631 (2023).
[21] E. R. Johnson, M. Salamone, M. Bietti, and G. A. DiLabio, "Modeling noncovalent radical–molecule interactions using conventional density-functional theory: Beware erroneous charge transfer," J. Phys. Chem. A **117**, 947–952 (2013).
[22] E. R. Johnson, A. Otero-de-la-Roza, and S. G. Dale, "Extreme density-driven delocalization error for a model solvated-electron system," J. Chem. Phys. **139**, 184116 (2013).
[23] M.-C. Kim, E. Sim, and K. Burke, "Ions in solution: Density corrected density functional theory (DC-DFT)," J. Chem. Phys. **140**, 18A528 (2014).
[24] W. A. Narvaez, D. M. Bartels, and W. H. Thompson, "Assessing the limitations of self-interaction-corrected functionals for describing the hydrated electron," J. Chem. Theory Comput. **22**, 5473–5483 (2026).
[25] B. Rana, M. P. Coons, and J. M. Herbert, "Detection and correction of delocalization errors for electron and hole polarons using density-corrected DFT," J. Phys. Chem. Lett. **13**, 5275–5284 (2022).
[26] B. Rana and J. M. Herbert, "Role of hemibonding in the structure and ultraviolet spectroscopy of the aqueous hydroxyl radical," Phys. Chem. Chem. Phys. **22**, 27829–27844 (2020).
[27] B. Rana and J. M. Herbert, "Hidden hemibonding in the aqueous hydroxyl radical," J. Phys. Chem. Lett. **12**, 8053–8060 (2021).
[28] B. Rana, G. J. O. Beran, and J. M. Herbert, "Correcting π-delocalisation errors in conformational energies using density-corrected DFT, with application to crystal polymorphs," Mol. Phys. **121**, e2138789 (2023).
[29] Y. Tawada, T. Tsuneda, S. Yanagisawa, T. Yanai, and K. Hirao, "A long-range corrected time-dependent density functional theory," J. Chem. Phys. **120**, 8425–8433 (2004).

23 October 2026 11:51:08

© Author(s) 2026

[30]O. A. Vydrov and G. E. Scuseria, "Assessment of a long-range corrected hybrid functional," J. Chem. Phys. **125**, 234109 (2006).
[31]T. M. Henderson, B. G. Janesko, and G. E. Scuseria, "Generalized gradient approximation model exchange holes for range-separated hybrids," J. Chem. Phys. **128**, 194105 (2008).
[32]A. W. Lange, M. A. Rohrdanz, and J. M. Herbert, "Charge-transfer excited states in a π-stacked adenine dimer, as predicted using long-range-corrected time-dependent density functional theory," J. Phys. Chem. B **112**, 6304–6308 (2008).
[33]M. A. Rohrdanz and J. M. Herbert, "Simultaneous benchmarking of ground- and excited-state properties with long-range-corrected density functional theory," J. Chem. Phys. **129**, 034107 (2008).
[34]M. A. Rohrdanz, K. M. Martins, and J. M. Herbert, "A long-range-corrected density functional that performs well for both ground-state properties and time-dependent density functional theory excitation energies, including charge-transfer excited states," J. Chem. Phys. **130**, 054112 (2009).
[35]T. Tsuneda and K. Hirao, "Long-range correction for density functional theory," Wiley Interdiscip. Rev.: Comput. Mol. Sci. **4**, 375–390 (2014).
[36]A. W. Lange and J. M. Herbert, "Both intra- and interstrand charge-transfer excited states in B-DNA are present at energies comparable to, or just above, the $^1\pi\pi^*$ excitonic bright states," J. Am. Chem. Soc. **131**, 3913–3922 (2009).
[37]C. M. Isborn, B. D. Mar, B. F. E. Curchod, I. Tavernelli, and T. J. Martínez, "The charge transfer problem in density functional theory calculations of aqueously solvated molecules," J. Phys. Chem. B **117**, 12189–12201 (2013).
[38]S. Kümmel, "Charge-transfer excitations: A challenge for time-dependent density functional theory that has been met," Adv. Energy Mater. **7**, 1700440 (2017).
[39]B. Alam, A. F. Morrison, and J. M. Herbert, "Charge separation and charge transfer in the low-lying excited states of pentacene," J. Phys. Chem. C **124**, 24653–24666 (2020).
[40]T. Stein, L. Kronik, and R. Baer, "Reliable prediction of charge transfer excitations in molecular complexes using time-dependent density functional theory," J. Am. Chem. Soc. **131**, 2818–2820 (2009).
[41]R. Baer, E. Livshits, and U. Salzner, "Tuned range-separated hybrids in density functional theory," Annu. Rev. Phys. Chem. **61**, 85–109 (2010).
[42]S. Refaely-Abramson, S. Sharifzadeh, N. Govind, J. Autschbach, J. B. Neaton, R. Baer, and L. Kronik, "Quasiparticle spectra from a nonempirical optimally tuned range-separated hybrid density functional," Phys. Rev. Lett. **109**, 226405 (2012).
[43]S. Refaely-Abramson, M. Jain, S. Sharifzadeh, J. B. Neaton, and L. Kronik, "Solid-state optical absorption from optimally tuned time-dependent range-separated hybrid density functional theory," Phys. Rev. B **92**, 081204(R) (2015).
[44]A. K. Manna, S. Refaely-Abramson, A. M. Reilly, A. Tkatchenko, J. B. Neaton, and L. Kronik, "Quantitative prediction of optical absorption in molecular solids from an optimally tuned screened range-separated hybrid functional," J. Chem. Theory Comput. **14**, 2919–2929 (2018).
[45]A. Mandal and J. M. Herbert, "Simplified tuning of long-range corrected time-dependent density functional theory," J. Phys. Chem. Lett. **16**, 2672–2680 (2025).
[46]J. M. Herbert, "Density-functional theory for electronic excited states," in *Theoretical and Computational Photochemistry: Fundamentals, Methods, Applications and Synergy with Experimental Approaches*, edited by C. García-Iriepa and M. Marazzi (Elsevier, Amsterdam, 2023), Chap. 3, pp. 69–118.
[47]N. A. Besley, M. J. G. Peach, and D. J. Tozer, "Time-dependent density functional theory calculations of near-edge X-ray absorption fine structure with short-range corrected functionals," Phys. Chem. Chem. Phys. **11**, 10350–10358 (2009).
[48]M. Gray, A. Mandal, and J. M. Herbert, "Revisiting the half-and-half functional," J. Phys. Chem. A **129**, 3969–3982 (2025).
[49]S. Dasgupta, B. Rana, and J. M. Herbert, "*Ab initio* investigation of the resonance Raman spectrum of the hydrated electron," J. Phys. Chem. B **123**, 8074–8085 (2019).
[50]P. Verma and R. J. Bartlett, "Increasing the applicability of density functional theory. IV. Consequences of ionization-potential improved exchange-correlation potentials," J. Chem. Phys. **140**, 18A534 (2014).
[51]D. S. Ranasinghe, J. T. Margraf, A. Perera, and R. J. Bartlett, "Vertical valence ionization potential benchmarks from equation-of-motion coupled cluster theory and QTP functionals," J. Chem. Phys. **150**, 074108 (2019).
[52]H. Kim, A. Perera, R. A. Mendes, and R. J. Bartlett, "Benchmarking ionization potentials and electron affinities of potential photovoltaic molecules using DFT/QTP functionals and EOM-CC," J. Chem. Phys. **163**, 174703 (2025).
[53]A. W. Duster, C.-H. Wang, C. M. Garza, D. E. Miller, and H. Lin, "Adaptive quantum/molecular mechanics: What have we learned, where are we, and where do we go from here?," Wiley Interdiscip. Rev.: Comput. Mol. Sci. **7**, e1310 (2017).
[54]Z. C. Holden, B. Rana, and J. M. Herbert, "Analytic energy gradients for the QM/MM-Ewald method using atomic charges derived from the electrostatic potential: Theory, implementation, and application to *ab initio* molecular dynamics of the aqueous electron," J. Chem. Phys. **150**, 144115 (2019).
[55]T. Giovannini and C. Cappelli, "Continuum vs. atomistic approaches to computational spectroscopy of solvated systems," Chem. Commun. **59**, 5644–5660 (2023).
[56]S. J. R. Lee, M. Welborn, F. R. Manby, and T. F. Miller, "Projection-based wavefunction-in-DFT embedding," Acc. Chem. Res. **52**, 1359–1368 (2019).
[57]K. Carter-Fenk, C. J. Mundy, and J. M. Herbert, "Natural charge-transfer analysis: Eliminating spurious charge-transfer states in time-dependent density functional theory via diabatization, with application to projection-based embedding," J. Chem. Theory Comput. **17**, 4195–4210 (2021).
[58]D. C. Claudino, R. L. Smith, and N. J. Mayhall, "Projection-based molecular quantum embedding via singular-value-informed orbital partitioning," in *Comprehensive Computational Chemistry*, edited by M. Yáñez and R. J. Boyd (Elsevier, 2024), Vol. 1, pp. 111–120.
[59]L. W. Chung, W. M. C. Sameera, R. Ramozzi, A. J. Page, M. Hatanaka, G. P. Petrova, T. V. Harris, X. Li, Z. Ke, F. Liu, H.-B. Li, L. Ding, and K. Morokuma, "The ONIOM method and its applications," Chem. Rev. **115**, 5678–5796 (2015).
[60]F. Libisch, C. Huang, and E. A. Carter, "Embedded correlated wavefunction schemes: Theory and applications," Acc. Chem. Res. **47**, 2768–2775 (2014).
[61]T. A. Wesolowski, S. Shedge, and X. Zhou, "Frozen-density embedding strategy for multilevel simulations of electronic structure," Chem. Rev. **115**, 5891–5928 (2015).
[62]M. Welborn, T. Tsuchimochi, and T. Van Voorhis, "Bootstrap embedding: An internally consistent fragment-based method," J. Chem. Phys. **145**, 074102 (2016).
[63]Q. Sun and G. K.-L. Chan, "Quantum embedding theories," Acc. Chem. Res. **49**, 2705–2712 (2016).
[64]D. V. Chulhai and J. D. Goodpaster, "Projection-based correlated wave function in density functional theory embedding for periodic systems," J. Chem. Theory Comput. **14**, 1928–1942 (2018).
[65]A. Goez and J. Neugebauer, "Embedding methods in quantum chemistry," in *Frontiers in Quantum Chemistry*, edited by M. J. Wójcik, H. Nakatsuji, B. Kirtman, and Y. Ozaki (Springer, Singapore, 2018), Chap. 7, pp. 139–180.
[66]L. O. Jones, M. A. Mosquera, G. C. Schatz, and M. A. Ratner, "Embedding methods for quantum chemistry: Applications from materials to life sciences," J. Am. Chem. Soc. **142**, 3281–3295 (2020).
[67]M. Nusspickel and G. H. Booth, "Systematic improvability in quantum embedding for real materials," Phys. Rev. X **12**, 011046–011061 (2022).
[68]C. R. Jacob and J. Neugebauer, "Subsystem density-functional theory (update)," Wiley Interdiscip. Rev.: Comput. Mol. Sci. **14**, e1700 (2024).
[69]N. Govind, Y. A. Wang, and E. A. Carter, "Electronic-structure calculations by first-principles density-based embedding of explicitly correlated systems," J. Chem. Phys. **110**, 7677–7688 (1999).
[70]T. Klüner, N. Govind, Y. A. Wang, and E. A. Carter, "Periodic density functional embedding theory for complete active space self-consistent field and configuration interaction calculations: Ground and excited states," J. Chem. Phys. **116**, 42–54 (2002).
[71]S. J. Nolan, M. J. Gillan, D. Alfè, N. L. Allan, and F. R. Manby, "Calculation of properties of crystalline lithium hydride using correlated wave function theory," Phys. Rev. B **80**, 165109–165116 (2009).
[72]O. Masur, M. Schütz, L. Maschio, and D. Usvyat, "Fragment-based direct-local-ring-coupled-cluster doubles treatment embedded in the periodic Hartree–Fock solution," J. Chem. Theory Comput. **12**, 5145–5156 (2016).
[73]F. Libisch, M. Marsman, J. Burgdörfer, and G. Kresse, "Embedding for bulk systems using localized atomic orbitals," J. Chem. Phys. **147**, 034110 (2017).
[74]M. Alessio, F. A. Bischoff, and J. Sauer, "Chemically accurate adsorption energies for methane and ethane monolayers on the MgO(001) surface," Phys. Chem. Chem. Phys. **20**, 9760–9769 (2018).

23 October 2026 11:51:08

© Author(s) 2026

[75]Z.-H. Cui, T. Zhu, and G. K.-L. Chan, "Efficient implementation of ab initio quantum embedding in periodic systems: Density matrix embedding theory," J. Chem. Theory Comput. **16**, 119–129 (2020).
[76]H. Q. Pham, M. R. Hermes, and L. Gagliardi, "Periodic electronic structure calculations with the density matrix embedding theory," J. Chem. Theory Comput. **16**, 130–140 (2020).
[77]H.-H. Lin, L. Maschio, D. Kats, D. Usvyat, and T. Heine, "Fragment-based restricted active space configuration interaction with second-order corrections embedded in periodic Hartree–Fock wavefunction," J. Chem. Theory Comput. **16**, 7100–7108 (2020).
[78]H. Ma, N. Sheng, M. Govoni, and G. Galli, "Quantum embedding theory for strongly correlated states in materials," J. Chem. Theory Comput. **17**, 2116–2125 (2021).
[79]T. Schäfer, F. Libisch, G. Kresse, and A. Grüneis, "Local embedding of coupled cluster theory into the random phase approximation using plane waves," J. Chem. Phys. **154**, 011101 (2021).
[80]M. T. Wachter-Lehn, K. Fink, and S. Höfener, "Wavefunction frozen-density embedding with one-dimensional periodicity: Electronic polarization effects from local perturbations," J. Chem. Phys. **157**, 134109–134124 (2022).
[81]M. Sharma and M. Sierka, "Efficient implementation of density functional theory based embedding for molecular and periodic systems using Gaussian basis functions," J. Chem. Theory Comput. **18**, 6892–6904 (2022).
[82]M. Schütz, L. Maschio, A. J. Karttunen, and D. Usvyat, "Exfoliation energy of black phosphorus revisited: A coupled cluster benchmark," J. Phys. Chem. Lett. **8**, 1290–1294 (2017).
[83]B. T. G. Lau, G. Knizia, and T. C. Berkelbach, "Regional embedding enables high-level quantum chemistry for surface science," J. Phys. Chem. Lett. **12**, 1104–1109 (2021).
[84]T. Schäfer, A. Gallo, A. Irmler, F. Hummel, and A. Grüneis, "Surface science using coupled cluster theory via local Wannier functions and in-RPA-embedding: The case of water on graphitic carbon nitride," J. Chem. Phys. **155**, 244103–244113 (2021).
[85]D. Rocca, J. F. Gonthier, J. Levin, T. Schäfer, A. Grüneis, H. W. Lee, and B. Kang, "Quantum simulation of carbon capture in periodic metal–organic frameworks," Digital Discovery **5**, 1388–1400 (2026).
[86]C. Rickert, L. Barta, E.-C. Flach, D. Kats, and D. Usvyat, "Application of the aperiodic defect model to a negatively charged monovacancy in phosphorene," J. Chem. Phys. **164**, 234118 (2026).
[87]P. J. Bygrave, N. L. Allan, and F. R. Manby, "The embedded many-body expansion for energetics of molecular crystals," J. Chem. Phys. **137**, 164102 (2012).
[88]D. R. Broderick, P. E. Bowling, C. Brandt, S. Childress, J. Shockey, J. Higley, H. Dickerson, S. S. Ahmed, and J. M. Herbert, "Fragme∩t: An open-source framework for multiscale quantum chemistry based on fragmentation," Wiley Interdiscip. Rev.: Comput. Mol. Sci. **15**, e70058 (2025).
[89]F. R. Manby, M. Stella, J. D. Goodpaster, and T. F. Miller III, "A simple, exact density-functional-theory embedding scheme," J. Chem. Theory Comput. **8**, 2564–2568 (2012).
[90]E. Monino, D. Drwal, M. Hapka, L. Veis, and K. Pernal, "Why projection-based WF-in-DFT cannot be exact, even with the exact exchange–correlation functional. Formal and practical sources of error," J. Chem. Phys. **164**, 224114 (2026).
[91]R. C. R. Pennifold, S. J. Bennie, T. F. Miller III, and F. R. Manby, "Correcting density-driven errors in projection-based embedding," J. Chem. Phys. **146**, 084113 (2017).
[92]A. Lange and J. M. Herbert, "Simple methods to reduce charge-transfer contamination in time-dependent density-functional calculations of clusters and liquids," J. Chem. Theory Comput. **3**, 1680–1690 (2007).
[93]E. Kolodzeiski and C. J. Stein, "Automated, consistent, and even-handed selection of active orbital spaces for quantum embedding," J. Chem. Theory Comput. **19**, 6643–6655 (2023).
[94]E. Kolodzeiski and C. J. Stein, "Efficient electronic-structure methods toward catalyst screening: Projection-based embedding theory for CO_2 reduction reaction intermediates," Angew. Chem., Int. Ed. **64**, e202503418 (2025).
[95]E. Epifanovsky, A. T. B. Gilbert, X. Feng, J. Lee, Y. Mao, N. Mardirossian, P. Pokhilko, A. F. White, M. P. Coons, A. L. Dempwolff, Z. Gan, D. Hait, P. R. Horn, L. D. Jacobson, I. Kaliman, J. Kussmann, A. W. Lange, K. U. Lao, D. S. Levine, J. Liu, S. C. McKenzie, A. F. Morrison, K. D. Nanda, F. Plasser, D. R. Rehn, M. L. Vidal, Z.-Q. You, Y. Zhu, B. Alam, B. J. Albrecht, A. Aldossary, E. Alguire, J. H. Andersen, V. Athavale, D. Barton, K. Begam, A. Behn, N. Bellonzi, Y. A. Bernard, E. J. Berquist, H. G. A. Burton, A. Carreras, K. Carter-Fenk, R. Chakraborty, A. D. Chien, K. D. Closser, V. Cofer-Shabica, S. Dasgupta, M. de Wergifosse, J. Deng, M. Diedenhofen, H. Do, S. Ehlert, P.-T. Fang, S. Fatehi, Q. Feng, T. Friedhoff, J. Gayvert, Q. Ge, G. Gidofalvi, M. Goldey, J. Gomes, C. E. González-Espinoza, S. Gulania, A. O. Gunina, M. W. D. Hanson-Heine, P. H. P. Harbach, A. Hauser, M. F. Herbst, M. Hernández Vera, M. Hodecker, Z. C. Holden, S. Houck, X. Huang, K. Hui, B. C. Huynh, M. Ivanov, Á. Jász, H. Ji, H. Jiang, B. Kaduk, S. Kähler, K. Khistyaev, J. Kim, G. Kis, P. Klunzinger, Z. Koczor-Benda, J. H. Koh, D. Kosenkov, L. Koulias, T. Kowalczyk, C. M. Krauter, K. Kue, A. Kunitsa, T. Kus, I. Ladjánszki, A. Landau, K. V. Lawler, D. Lefrancois, S. Lehtola, R. R. Li, Y.-P. Li, J. Liang, M. Liebenthal, H.-H. Lin, Y.-S. Lin, F. Liu, K.-Y. Liu, M. Loipersberger, A. Luenser, A. Manjanath, P. Manohar, E. Mansoor, S. F. Manzer, S.-P. Mao, A. V. Marenich, T. Markovich, S. Mason, S. A. Maurer, P. F. McLaughlin, M. F. S. J. Menger, J.-M. Mewes, S. A. Mewes, P. Morgante, J. W. Mullinax, K. J. Oosterbaan, G. Paran, A. C. Paul, S. K. Paul, F. Pavošević, Z. Pei, S. Prager, E. I. Proynov, Á. Rák, E. Ramos-Cordoba, B. Rana, A. E. Rask, A. Rettig, R. M. Richard, F. Rob, E. Rossomme, T. Scheele, M. Scheurer, M. Schneider, N. Sergueev, S. M. Sharada, W. Skomorowski, D. W. Small, C. J. Stein, Y.-C. Su, E. J. Sundstrom, Z. Tao, J. Thirman, G. J. Tornai, T. Tsuchimochi, N. M. Tubman, S. P. Veccham, O. Vydrov, J. Wenzel, J. Witte, A. Yamada, K. Yao, S. Yeganeh, S. R. Yost, A. Zech, I. Y. Zhang, X. Zhang, Y. Zhang, D. Zuev, A. Aspuru-Guzik, A. T. Bell, N. A. Besley, K. B. Bravaya, B. R. Brooks, D. Casanova, J.-D. Chai, S. Coriani, C. J. Cramer, G. Cserey, A. E. DePrince III, R. A. DiStasio, Jr., A. Dreuw, B. D. Dunietz, T. R. Furlani, W. A. Goddard III, S. Hammes-Schiffer, T. Head-Gordon, W. J. Hehre, C.-P. Hsu, T.-C. Jagau, Y. Jung, A. Klamt, J. Kong, D. S. Lambrecht, W. Liang, N. J. Mayhall, C. W. McCurdy, J. B. Neaton, C. Ochsenfeld, J. A. Parkhill, R. Peverati, V. A. Rassolov, Y. Shao, L. V. Slipchenko, T. Stauch, R. P. Steele, J. E. Subotnik, A. J. W. Thom, A. Tkatchenko, D. G. Truhlar, T. Van Voorhis, T. A. Wesolowski, K. B. Whaley, H. L. Woodcock III, P. M. Zimmerman, S. Faraji, P. M. W. Gill, M. Head-Gordon, J. M. Herbert, and A. I. Krylov, "Software for the frontiers of quantum chemistry: An overview of developments in the Q-Chem 5 package," J. Chem. Phys. **155**, 084801 (2021).
[96]T. D. Kühne, M. Iannuzzi, M. Del Ben, V. V. Rybkin, P. Seewald, F. Stein, T. Laino, R. Z. Khaliullin, O. Schütt, F. Schiffmann, D. Golze, J. Wilhelm, S. Chulkov, M. H. Bani-Hashemian, V. Weber, U. Borštnik, M. Taillefumier, A. S. Jakobovits, A. Lazzaro, H. Pabst, T. Müller, R. Schade, M. Guidon, S. Andermatt, N. Holmberg, G. K. Schenter, A. Hehn, A. Bussy, F. Belleflamme, G. Tabacchi, A. Glöß, M. Lass, I. Bethune, C. J. Mundy, C. Plessl, M. Watkins, J. VandeVondele, M. Krack, and J. Hutter, "CP2K: An electronic structure and molecular dynamics software package—Quickstep: Efficient and accurate electronic structure calculations," J. Chem. Phys. **152**, 194103 (2020).
[97]A. Bussy and J. Hutter, "Efficient periodic resolution-of-the-identity Hartree–Fock exchange method with k-point sampling and Gaussian basis sets," J. Chem. Phys. **160**, 064116 (2024).
[98]V. Alizadeh, J. Pototschnig, L. M. Seidler, S. Ehlert, and T. D. Kühne, "Periodic GFN2-xTB in CP2K: Multipolar Ewald electrostatics, k-point sampling, and transferability benchmarks for molecular solids," J. Chem. Theory Comput. **22**, 9688–9699 (2026).
[99]M. Guidon, J. Hutter, and J. VandeVondele, "Robust periodic Hartree–Fock exchange for large-scale simulations using Gaussian basis sets," J. Chem. Theory Comput. **5**, 3010–3021 (2009).
[100]M. Guidon, J. Hutter, and J. VandeVondele, "Auxiliary density matrix methods for Hartree–Fock exchange calculations," J. Chem. Theory Comput. **6**, 2348–2364 (2010).
[101]C. Adriaanse, J. Cheng, V. Chau, M. Sulpizi, J. VandeVondele, and M. Sprik, "Aqueous redox chemistry and the electronic band structure of liquid water," J. Phys. Chem. Lett. **3**, 3411–3415 (2012).
[102]J. Cheng and M. Sprik, "Alignment of electronic energy levels at electrochemical interfaces," Phys. Chem. Chem. Phys. **14**, 11245–11267 (2012).
[103]F. Ambrosio, G. Miceli, and A. Pasquarello, "Redox levels in aqueous solution: Effect of van der Waals interactions and hybrid functionals," J. Chem. Phys. **143**, 244508 (2015).
[104]C. Zhang, F. Tang, M. Chen, J. Xu, L. Zhang, D. Y. Qiu, J. P. Perdew, M. L. Klein, and X. Wu, "Modeling liquid water by climbing up Jacob's ladder in density functional theory facilitated by using deep neural network potentials," J. Phys. Chem. B **125**, 11444–11456 (2021).

23 October 2026 11:51:08

© Author(s) 2026

[105]A. Bernas, C. Ferradini, and J.-P. Jay-Gerin, "On the electronic structure of liquid water: Facts and reflections," Chem. Phys. **222**, 151–160 (1997).
[106]J. V. Coe, A. D. Earhart, M. H. Cohen, G. J. Hoffman, H. W. Sarkas, and K. H. Bowen, "Using cluster studies to approach the electronic structure of bulk water: Reassessing the vacuum level, conduction band edge, and band gap of water," J. Chem. Phys. **107**, 6023–6031 (1997).
[107]C. Fang, W.-F. Li, R. S. Koster, J. Klimeš, A. van Blaaderen, and M. A. van Huis, "The accurate calculation of the band gap of liquid water by means of *GW* corrections applied to plane-wave density functional theory molecular dynamics simulations," Phys. Chem. Chem. Phys. **17**, 365–375 (2015).
[108]J. D. Gouveia and J. Coutinho, "Can we rely on hybrid-DFT energies of solid-state problems with local-DFT geometries?," Electron. Struct. **1**, 015008 (2019).
[109]B. Hégely, P. R. Nagy, G. G. Ferenczy, and M. Kállay, "Exact density functional and wave function embedding schemes based on orbital localization," J. Chem. Phys. **145**, 064107 (2016).
[110]S. Huzinaga and A. A. Cantu, "Theory of separability of many-electron systems," J. Chem. Phys. **55**, 5543–5549 (1971).
[111]J. M. Herbert and M. Head-Gordon, "Curvy-steps approach to constraint-free extended-Lagrangian *ab initio* molecular dynamics, using atom-centered basis functions: Convergence toward Born-Oppenheimer trajectories," J. Chem. Phys. **121**, 11542–11556 (2004).
[112]J. Pipek and P. G. Mezey, "A fast intrinsic localization procedure applicable for *ab initio* and semiempirical linear combination of atomic orbital wave functions," J. Chem. Phys. **90**, 4916–4926 (1989).
[113]I.-M. Høyvik, B. Jansik, and P. Jørgensen, "Pipek–Mezey localization of occupied and virtual orbitals," J. Comput. Chem. **34**, 1456–1462 (2013).
[114]D. Claudino and N. J. Mayhall, "Automatic partition of orbital spaces based on singular value decomposition in the context of embedding theories," J. Chem. Theory Comput. **15**, 1053–1064 (2019).
[115]E. Ö. Jónsson, S. Lehtola, M. Puska, and H. Jónsson, "Theory and applications of generalized Pipek–Mezey Wannier functions," J. Chem. Theory Comput. **13**, 460–474 (2017).
[116]M. C. Clement, X. Wang, and E. F. Valeev, "Robust Pipek–Mezey orbital localization in periodic solids," J. Chem. Theory Comput. **17**, 7406–7415 (2021).
[117]A. Sanchez de Meras, M.-B. Lepetit, and J.-P. Malrieu, "Discontinuity of valence CASSCF wave functions around weakly avoided crossing between valence configurations," Chem. Phys. Lett. **172**, 163–168 (1990).
[118]A. Zaitsevskii and J.-P. Malrieu, "The discontinuities of state-average MCSCF potential surfaces," Chem. Phys. Lett. **228**, 458–462 (1994).
[119]L. N. Tran and E. Neuscamman, "Improving excited-state potential energy surfaces via optimal orbital shapes," J. Phys. Chem. A **124**, 8273–8279 (2020).
[120]I. A. Zaporozhets, V. V. Ivanov, D. I. Lyakh, and L. Adamowicz, "Discontinuities-free complete-active-space state–specific multi-reference coupled cluster theory for describing bond stretching and dissociation," J. Chem. Phys. **143**, 024109 (2015).
[121]B. G. Levine, A. S. Durden, M. P. Esch, F. Liang, and Y. Shu, "CAS without SCF—Why to use CASCI and where to get the orbitals," J. Chem. Phys. **154**, 090902 (2021).
[122]A. Marie and H. G. A. Burton, "Excited states, symmetry breaking, and unphysical solutions in state-specific CASSCF theory," J. Phys. Chem. A **127**, 4538–4552 (2023).
[123]S. Saade and H. G. A. Burton, "Excited state-specific CASSCF theory for the torsion of ethylene," J. Chem. Theory Comput. **20**, 5105–5114 (2024).
[124]Q. Wang, V. Agarawal, M. R. Hermes, M. Motta, J. E. Rice, G. O. Jones, and L. Gagliardi, "Distinguishing homolytic vs heterolytic bond dissociation of phenylsulfonium cations with localized active space methods," J. Chem. Phys. **161**, 014106 (2024).
[125]W. J. Glover, "Communication: Smoothing out excited-state dynamics: Analytical gradients for dynamically weighted complete active space self-consistent field," J. Chem. Phys. **141**, 171102 (2014).
[126]M. Welborn, F. R. Manby, and T. F. Miller III, "Even-handed subsystem selection in projection-based embedding," J. Chem. Phys. **149**, 144101 (2018).
[127]M. Bensberg and J. Neugebauer, "Direct orbital selection for projection-based embedding," J. Chem. Phys. **150**, 214106 (2019).
[128]J. M. Herbert, Y. Zhu, B. Alam, and A. K. Ojha, "Time-dependent density functional theory for x-ray absorption spectra: Comparing the real-time approach to linear response," J. Chem. Theory Comput. **19**, 6745–6760 (2023).
[129]D. Claudino and N. J. Mayhall, "Simple and efficient truncation of virtual spaces in embedded wave functions via concentric localization," J. Chem. Theory Comput. **15**, 6085–6096 (2019).
[130]X. Liu, K. D. Nanda, J. Liang, and M. Head-Gordon, "Efficient, precise DFT calculations of NMR shieldings: Revisiting the finite field approach," arXiv:2608.24655 (2026).
[131]P. Vassilev, M. J. Louwerse, and E. J. Baerends, "Ab initio molecular dynamics simulation of the $OH^{\bullet}$ radical in liquid water," Chem. Phys. Lett. **398**, 212–216 (2004).
[132]J. M. Khalack and A. P. Lyubartsev, "Solvation structure of hydroxyl radical by Car–Parrinello molecular dynamics," J. Phys. Chem. A **109**, 378–386 (2005).
[133]E. Codorniu-Hernández and P. G. Kusalik, "Insights into the solvation and mobility of the hydroxyl radical in aqueous solution," J. Chem. Theory Comput. **7**, 3725–3732 (2011).
[134]E. Codorniu-Hernández and P. G. Kusalik, "Mobility mechanism of hydroxyl radicals in aqueous solution via hydrogen transfer," J. Am. Chem. Soc. **134**, 532–538 (2012).
[135]E. Codorniu-Hernández, A. D. Boese, and P. G. Kusalik, "The hemibond as an alternative condensed phase structure for the hydroxyl radical," Can. J. Chem. **91**, 544–551 (2013).
[136]D. M. Chipman, "Hemibonding between hydroxyl radical and water," J. Phys. Chem. A **115**, 1161–1171 (2011).
[137]J. VandeVondele and M. Sprik, "A molecular dynamics study of the hydroxyl radical in solution applying self-interaction-corrected density functional methods," Phys. Chem. Chem. Phys. **7**, 1363–1367 (2005).
[138]C. Apostolidou, "OH radical in water from *ab initio* molecular dynamics simulation employing hybrid functionals," J. Chem. Phys. **151**, 064111 (2019).
[139]C. Apostolidou, "Vibrational spectra of the OH radical in water: Ab initio molecular dynamics simulations and quantum chemical calculations using hybrid functionals," Adv. Theory Simul. **3**, 2000174 (2020).
[140]P. Pulay, "Convergence acceleration of iterative sequences. The case of SCF iteration," Chem. Phys. Lett. **73**, 393–398 (1980).
[141]A. V. Marenich, S. V. Jerome, C. J. Cramer, and D. G. Truhlar, "Charge model 5: An extension of Hirshfeld population analysis for the accurate description of molecular interactions in gaseous and condensed phases," J. Chem. Theory Comput. **8**, 527–541 (2012).
[142]A. Mandal, E. J. Berquist, and J. M. Herbert, "A new parameterization of the DFT/CIS method with applications to core-level spectroscopy," J. Chem. Phys. **161**, 044114 (2024).
[143]S. Pellerin, J. M. Cormier, F. Richard, K. Musiol, and J. Chapelle, "A spectroscopic diagnostic method using UV OH band spectrum," J. Phys. D: Appl. Phys. **29**, 726 (1996).
[144]J. M. Herbert, "Visualizing and characterizing excited states from time-dependent density functional theory," Phys. Chem. Chem. Phys. **26**, 3755–3794 (2024).
[145]J. Hutter, "Excited state nuclear forces from the Tamm–Dancoff approximation to time-dependent density functional theory within the plane wave basis set framework," J. Chem. Phys. **118**, 3928–3934 (2003).
[146]A.-S. Hehn, B. Sertcan, F. Belleflamme, S. K. Chulkov, M. B. Watkins, and J. Hutter, "Excited-state properties for extended systems: Efficient hybrid density functional methods," J. Chem. Theory Comput. **18**, 4186–4202 (2022).
[147]B. S. Gökmen, J. Hutter, and A.-S. Hehn, "Excited-state forces with the Gaussian and augmented plane wave method for the Tamm–Dancoff approximation of time-dependent density functional theory," J. Chem. Theory Comput. **20**, 8494–8504 (2024).
[148]G. Czapski and B. H. J. Bielski, "Absorption spectra of the $^{\bullet}OH$ and $O^{\bullet-}$ radicals in aqueous solutions," Radiat. Phys. Chem. **41**, 503–505 (1993).
[149]S. J. Bennie, B. F. E. Curchod, F. R. Manby, and D. R. Glowacki, "Pushing the limits of EOM-CCSD with projector-based embedding for excitation energies," J. Phys. Chem. Lett. **8**, 5559–5565 (2017).

23 October 2026 11:51:08

© Author(s) 2026

[150]J. Wang, P. Cieplak, and P. A. Kollman, "How well does a restrained electrostatic potential (RESP) model perform in calculating conformational energies of organic and biological molecules?," J. Comput. Chem. **21**, 1049–1074 (2000).
[151]F. Ambrosio, G. Miceli, and A. Pasquarello, "Structural, dynamical, and electronic properties of liquid water: A hybrid functional study," J. Phys. Chem. B **120**, 7456–7470 (2016).
[152]E. Epifanovsky, K. Kowalski, P.-D. Fang, M. Valiev, S. Matsika, and A. I. Krylov, "On the electronically excited states of uracil," J. Phys. Chem. A **112**, 9983–9992 (2008).
[153]X. Zhang and J. M. Herbert, "Excited-state deactivation pathways in uracil versus hydrated uracil: Solvatochromatic shift in the $^1n\pi^*$ state is the key," J. Phys. Chem. B **118**, 7806–7817 (2014).
[154]P. Liao and E. A. Carter, "Optical excitations in hematite (α-Fe_2O_3) via embedded cluster models: A CASPT2 study," J. Phys. Chem. C **115**, 20795–20805 (2011).
[155]P. Liao, M. C. Toroker, and E. A. Carter, "Electron transport in pure and doped hematite," Nano Lett. **11**, 1775–1781 (2011).
[156]P. Liao and E. A. Carter, "Hole transport in pure and doped hematite," J. Appl. Phys. **112**, 013701 (2012).
[157]A. Kubas, M. Verkamp, J. Vura-Weis, F. Neese, and D. Maganas, "Restricted open-shell configuration interaction singles study on M- and L-edge x-ray absorption spectroscopy of solid chemical systems," J. Chem. Theory Comput. **14**, 4320–4334 (2018).
[158]T. N. Mihm, B. Yang, and J. J. Shepherd, "Power laws used to extrapolate the coupled cluster correlation energy to the thermodynamic limit," J. Chem. Theory Comput. **17**, 2752–2758 (2021).
[159]T. N. Mihm, W. Z. Van Benshoten, and J. J. Shepherd, "Accelerating convergence to the thermodynamic limit with twist angle selection applied to methods beyond many-body perturbation theory," J. Chem. Phys. **154**, 024113 (2021).
[160]T. N. Mihm, T. Schäfer, S. K. Ramadugu, L. Weiler, A. Grüneis, and J. J. Shepherd, "A shortcut to the thermodynamic limit for quantum many-body calculations of metals," Nat. Comput. Sci. **1**, 801–808 (2021).
[161]T. N. Mihm, L. Weiler, and J. J. Shepherd, "How the exchange energy can affect power laws used to extrapolate the coupled cluster correlation energy to the thermodynamic limit," J. Chem. Theory Comput. **19**, 1686–1697 (2023).
[162]X. Xing and L. Lin, "Inverse volume scaling of finite-size errors in periodic coupled cluster theory," Phys. Rev. X **14**, 011059 (2024).
[163]S. J. Quiton, J. D. F. Pottecher, M. Head-Gordon, and L. Lin, "Reduction of finite-size effects for second-order Møller–Plesset perturbation theory with singularity subtraction," arXiv:2605.12727 (2026).
[164]H.-Z. Ye and T. C. Berkelbach, "Wavefunction-based periodic quantum chemistry," arXiv:2607.28554 (2026).
[165]D. V. Chulhai and J. D. Goodpaster, "Improved accuracy and efficiency in quantum embedding through absolute localization," J. Chem. Theory Comput. **13**, 1503–1508 (2017).
[166]D. Hu, W. Ho, X. Chen, S. Wang, and W. A. Goddard III, "Nonthermally accessible phase for CO on the Si(100) surface," Phys. Rev. Lett. **78**, 1178–1181 (1997).
[167]D. Traore, J. Toulouse, and E. Giner, "Accelerated basis-set convergence of coupled-cluster excitation energies using the density-based basis-set correction method," Faraday Discuss. **254**, 315–331 (2024).
[168]A. D. Laurent, A. Blondel, and D. Jacquemin, "Choosing an atomic basis set for TD-DFT, SOPPA, ADC(2), CIS(D), CC2, and EOM-CCSD calculations of low-lying excited states of organic dyes," Theor. Chem. Acc. **134**, 76 (2015).
[169]J. VandeVondele and J. Hutter, "Gaussian basis sets for accurate calculations on molecular systems in gas and condensed phases," J. Chem. Phys. **127**, 114105 (2007).
[170]R. Pasquier, M. Grami, and J. Wilhelm, "Gaussian basis sets for all-electron excited-state calculations of large molecules," J. Chem. Theory Comput. **22**, 540–557 (2026).
[171]E. Giner, B. Pradines, A. Ferté, R. Assaraf, A. Savin, and J. Toulouse, "Curing basis-set convergence of wave-function theory using density-functional theory: A systematically improvable approach," J. Chem. Phys. **149**, 194301 (2018).
[172]D. Traore, E. Giner, and J. Toulouse, "Basis-set correction based on density-functional theory: Linear-response formalism for excited-state energies," J. Chem. Phys. **158**, 234107 (2023).
[173]Ohio Supercomputer Center, http://osc.edu/ark:/19495/f5s1ph73 (accessed 20 September 2026).

23 October 2026 11:51:08

© Author(s) 2026